RIVISTA DEL NUOVO CIMENTO Vol. 41, N. 6 2018
DOI 10.1393/ncr/i2018-10148-8

High-precision innovative sensing with continuous-variable optical states

Stefano Olivares([1])([2])([*])

([1]) *Quantum Technology Lab, Dipartimento di Fisica "Aldo Pontremoli", Università degli Studi di Milano - via Celoria 16, I-20133 Milano, Italy*
([2]) *INFN, Sezione di Milano - via Celoria 16, I-20133 Milano, Italy*

received 19 February 2018

Summary. — When applied to practical problems, the very laws of quantum mechanics can provide a unique resource to beat the limits imposed by classical physics: this is the case of quantum metrology and high-precision sensing. Here we review the main results obtained in the recent years at the Quantum Technology Lab of the Department of Physics "Aldo Pontremoli" of the University of Milan, also in collaboration with national and international institutions. In particular we focus on the application of continuous-variable optical quantum states and operations to improve different fields of research, ranging from interferometry to more fundamental problems, such as the testing of quantum gravity.

([*]) E-mail: stefano.olivares@fisica.unimi.it

1. – Introduction

Quantum states of the radiation field represent a key ingredient to beat the limits imposed by classical light. The possibility to generate and manipulate single-photon states [1, 2] has made the implementation of protocols beyond the possibility of classical physical systems possible, paving the way to quantum cryptography [3], quantum communication [4], quantum enhanced sensing and metrology [5,6] and the study of complex problems as, for instance, the boson sampling [7,8]. When single photons are considered, the information is usually encoded into observables with a discrete spectrum, such as the polarisation degree of freedom. Unfortunately, the information encoded in single-photon states may be completely destroyed by the presence of losses: once the photon is lost, the carried information cannot be retrieved, though one can resort to schemes more tolerant to dissipation [9].

Therefore, many efforts have been made to extend discrete-variable quantum information protocols to the continuous-variable analogue, where the information is now encoded into observables with continuous spectrum (but not only), such as the amplitude or the phase of the field [10, 11]. Continuous-variable optical states are usually more robust to losses with respect to the single photons [12, 13], since they may contain mesoscopic [14] or macroscopic number of photons [15, 16].

In this scenario, optical correlations, both quantum and classical, represent a fundamental resource for developing technologies, opening unprecedented opportunities in the fields of metrology, positioning, imaging and sensing. Furthermore, the correlations existing between two or more [17] light beams have also a theoretical interest, being of key relevance in quantum optics and quantum electrodynamics and are at the basis of the quantum information processing.

In this paper we are going to summarise some of the main theoretical and experimental results we achieved at the Quantum Technology Lab of the Department of Physics "Aldo Pontremoli" of University of Milan also in collaboration with national and international teams. We will focus on our research on optical continuous-variable states and their application to interferometry, imaging and also to test more fundamental theories, such as the noncommutativity of position and momentum at the Planck scale.

The structure of the paper is as follows. Section **2** introduces the basic tools of the estimation and quantum estimation theory and, in particular, the role of the Fisher and quantum Fisher information.

In sect. **3** we will see how it is possible to enhance the sensitivity of an interferometer exploiting the quantum features of light. We present the main results we obtained when continuous-variable states, such as coherent and squeezed states of the optical field, are used to feed the interferometers: this will be the subject of sect. **4**, where we will study the bound imposed by quantum mechanics to the precision of an interferometer when only continuous-variable optical states are considered.

Quantum correlations can be exploited to improve the detection. In sect. **5** we present the first realisation of a practical quantum illumination protocol. It is a scheme to detect the presence of a faint object embedded in a noisy background, exploiting the quantum correlation existing between two light beams.

The possibility to enhance the sensitivity of optical interferometers by using setups based on two interferometers instead of a single one, is discussed in sects. **6**, **7** and **8**. In sect. **7** we show how two correlated interferometers can be used to test quantum gravity and, more precisely, the noncommutativity of position and momentum at the Planck scale, outperforming schemes based on classical light. Section **8** investigates the role

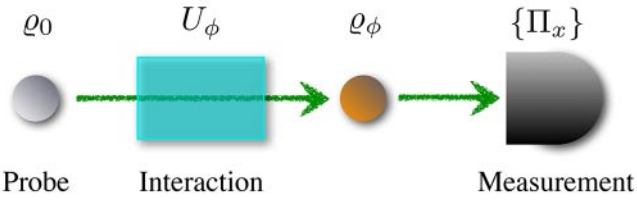

Fig. 1. – Scheme of a quantum estimation protocol: a quantum probe is prepared in the initial state ϱ_0 and interacts with a system. The interaction, described by the unitary operator U_ϕ, is characterised by the parameter ϕ we want to estimate. The evolved state is measured and the outcomes are processed to retrieve the information about ϕ. In general the measurement is described by a positive operator-valued measure (POVM) $\{\Pi_x\}$, where x is the outcome. See the text for details.

of a nonclassical resource, such as squeezing, to improve the performance of correlated interferometry. Finally, we draw some concluding remarks in sect. **9**.

Throughout the manuscript we will use many concepts from quantum optics. The interested reader can find a brief review of these basic notions in dedicated appendices.

2. – Basics of quantum estimation theory

In this section we review the basic tools of estimation theory and quantum estimation theory which we will use throughout this paper. In particular, we will introduce the concepts of Fisher information and of quantum Fisher information.

When a physical parameter is not directly accessible, one needs to resort to indirect measurements. This is the case, for instance, of the measurement of a phase shift, of the entropy or of the entanglement between two or more parties of a quantum system. Here we focus on the single-parameter estimation but our results can be extended to scenarios involving more than one parameter [18].

In fig. 1 we sketch a typical setup to estimate one parameter, say ϕ, through a quantum probe. In a quantum estimation protocol, a quantum probe is prepared in a known state described by the density operator ϱ_0. Then the probe interacts with a system, the interaction being described by the unitary operator U_ϕ. The evolved state of the probe, $\varrho_\phi = U_\phi \varrho_0 U_\phi^\dagger$, encodes the unknown parameter ϕ and, then, undergoes a measurement described in general by the positive operator-valued measure (POVM) $\{\Pi_x\}$, x being the measurement outcome. The data sample $\Omega = \{x_1, x_2, \ldots, x_M\}$ is finally processed to retrieve the value of the parameter by means of a suitable estimator $\hat{\phi}$. Of course, we are not only interested in the expectation value $E[\hat{\phi}]$ of $\hat{\phi}$, but also in its uncertainty $\mathrm{var}(\hat{\phi}) = E[\hat{\phi}^2] - E[\hat{\phi}]^2$. Therefore, the main goals of quantum estimation theory are to find the *optimal probes* which minimise the uncertainty and the *optimal measurements* which allow to reach such minimum uncertainty.

From the classical point of view, optimal unbiased estimators saturate the Cramér-Rao inequality or bound [19]

$$\mathrm{var}(\hat{\phi}) \geq \frac{1}{MF(\phi)}\,, \tag{1}$$

and we introduced the *Fisher information*

$$F(\phi) = \sum_{k=1}^{M} p(x_k|\phi)\,[\partial_\phi \log p(x_k|\phi)]^2, \tag{2}$$

$p(x|\phi)$ being the conditional probability of the outcome x given ϕ.

In the presence of a quantum probe and of a POVM, the conditional probability reads

$$p(x|\phi) = \mathrm{Tr}[\varrho_\phi \Pi_x], \tag{3}$$

and, thus, the Fisher information can be written as (to be more general, we assume that $x \in \Omega \subset \mathbb{R}$)

$$F(\phi) = \int_\Omega \frac{\mathrm{Tr}[\partial_\phi \varrho_\phi \Pi_x]^2}{\mathrm{Tr}[\varrho_\phi \Pi_x]}\,\mathrm{d}x, \tag{4a}$$

$$= \int_\Omega \frac{\Re\mathrm{e}\{\mathrm{Tr}[\varrho_\phi \Pi_x L_\phi]\}^2}{\mathrm{Tr}[\varrho_\phi \Pi_x]}\,\mathrm{d}x, \tag{4b}$$

where L_ϕ is the symmetric logarithmic derivative such that

$$\frac{\partial \varrho_\phi}{\partial \phi} = \frac{L_\phi \varrho_\phi + \varrho_\phi L_\phi}{2}\,. \tag{5}$$

We can now maximise $F(\phi)$ over all the possible POVMs to obtain the quantum Cramér-Rao bound [20, 21]

$$\mathrm{var}(\hat{\phi}) \geq \frac{1}{M H(\phi)}\,, \tag{6}$$

where $H(\phi) = \mathrm{Tr}[\varrho_\phi L_\phi^2] \geq F(\phi)$ is the *quantum Fisher information* [19, 22]. According to its definition, the eigenvectors of the symmetric logarithmic derivative L_ϕ correspond to the optimal POVM.

Looking for the analytical expression of the POVM and the optimal measurement is not always a simple task, since it requires an optimisation procedure. However, there are many cases in which it is possible to find some explicit relations.

In the simplest scenario the parameter to be estimated is the amplitude of a unitary perturbation applied to the probe state ϱ_0. This is the case, for instance, of a phase shift imposed to an optical field. If $\mathcal{G}$ is the Hermitian generator of the perturbation, we can write $U_\phi = \exp(-i\,\phi\,\mathcal{G})$. Now, expanding the input state in its eigenbasis, namely

$$\varrho_0 = \sum_n \varrho_n |\psi_n\rangle\langle\psi_n|, \tag{7}$$

we obtain $\varrho_\phi = \sum_n \varrho_n |\psi_n^{(\phi)}\rangle\langle\psi_n^{(\phi)}|$, with $|\psi_n^{(\phi)}\rangle = U_\phi|\psi_n\rangle$. It is straightforward to show that [18]

$$H = 2 \sum_{n \neq m} \frac{(\varrho_n - \varrho_m)^2}{\varrho_n + \varrho_m} |\langle\psi_n|\mathcal{G}|\psi_m\rangle|^2, \tag{8}$$

and it is independent of ϕ. Moreover, if the input state is a pure state, *i.e.* $\varrho_0 = |\psi_0\rangle\langle\psi_0|$, eq. (8) reduces to

$$H = 4\left(\langle\psi_0|\mathcal{G}^2|\psi_0\rangle - \langle\psi_0|\mathcal{G}|\psi_0\rangle^2\right), \tag{9a}$$

$$= 4\,\mathrm{var}[\mathcal{G}], \tag{9b}$$

namely, the quantum Fisher information is proportional to the fluctuations of the generator $\mathcal{G}$ on the probe state.

In sects. **3** and **4** we will apply these results to find the ultimate bounds to interferometric sensitivity. The interested reader can find in refs. [18] and [23] further details about the application of quantum estimation theory to more general scenarios of interest for quantum information processing. In particular, at our Quantum Technology Lab we applied the tools of quantum estimation to quantum optics [24-26], to open quantum systems [27-29] and to more fundamental problems [30-32], just to cite some of the relevant fields of research we investigated in the last years.

3. – Quantum interferometry with continuous-variable states

In this section we introduce the reader to optical quantum interferometry using the sensitivity of a typical interferometer and its connection with the Fisher information. The application of quantum estimation theory to find the ultimate bounds given by the quantum Fisher information and the analysis of more sophisticated setups, involving also active elements, will be discussed in sect. **4**.

An optical interferometer is a paradigmatic example of one of the most precise devices available in physics. Its applications range from technological ones, to the challenging task of modern cosmology, *i.e.* the direct detection of gravitational waves, and also to measure Planck-scale effects predicted by quantum gravity theories. An interferometer should maximise the precision in the estimation of phase-shift fluctuations given some energy constraints on the energy circulating in the interferometer itself. To this aim one can exploit the nonclassical features of the probe beams which may outperform the performance of the corresponding classical ones, thus leaving room for quantum enhanced interferometry. However, the fluctuations associated with the very quantum nature of light pose bounds to the precision, which can be assessed by the modern tools of quantum estimation theory briefly introduced in sect. **2**.

The key ingredient of an optical interferometers is the beam splitter, a linear optical device in which two beams of light interfere (see appendix A). In fig. 2 we sketched a Mach-Zehnder interferometer, but analogous results can be obtained in the case of a Michelson interferometer. The two input field modes, described by the annihilation operators a and b, with $[a, a^\dagger] = \mathbb{I}$ and $[b, b^\dagger] = \mathbb{I}$, evolve into the output modes c and d which depend on the phase ϕ. To find the input-output relations, we should transform the input modes through the first 50:50 beam splitter, then apply the phase shift and the reflections at the mirrors and, finally, recombine the resulting modes in a second 50:50 beam splitter.

Besides the final measurement, it is interesting to note that, from the theoretical point of view, any interferometer measuring a phase shift ϕ can be summarised by two input light beams which interfere at a beam splitter with transmissivity $\tau = \cos^2(\phi/2)$, as sketched in fig. 3. In the case of the Mach-Zehnder interferometer of fig. 2, this requires to add two phase shifters at $\pi/2$ (see PhS in fig. 2). In this view, as the reader can verify applying the transformations associated with the beam splitter, with the mirror

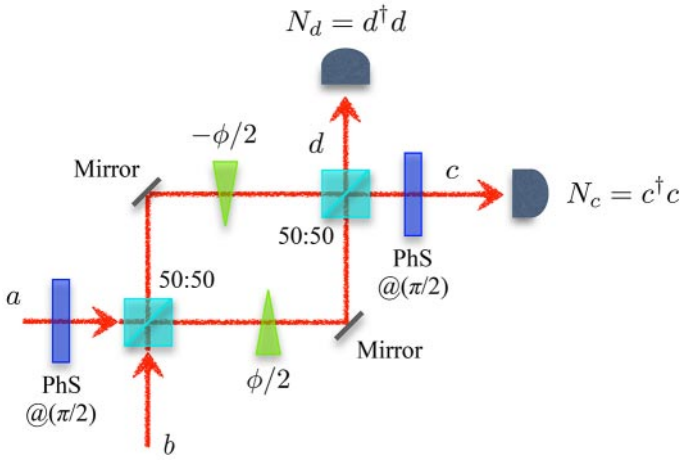

Fig. 2. – Scheme of a Mach-Zehnder interferometer. The two input modes, described by the annihilation operators a and b, with $[a, a^\dagger] = \mathbb{I}$ and $[b, b^\dagger] = \mathbb{I}$, interfere at a first 50:50 beam splitter and an overall phase-shift difference ϕ between the beams is applied. The two beams are then recombined at a second 50:50 beam splitter and, finally, they are detected by measuring the number of photons $N_c = c^\dagger c$ and $N_d = d^\dagger d$, respectively, where c and d are the annihilation operators of the output fields, $[c, c^\dagger] = \mathbb{I}$ and $[d, d^\dagger] = \mathbb{I}$. In the scheme we also added two phase shifters (PhS) at a fixed phase $\pi/2$: this allows to describe the whole evolution of the input modes through the interferometer as a simpler one in which they interfere at a single beam splitter with transmissivity $\tau(\phi) = \cos^2(\phi/2)$, as shown in fig. 3.

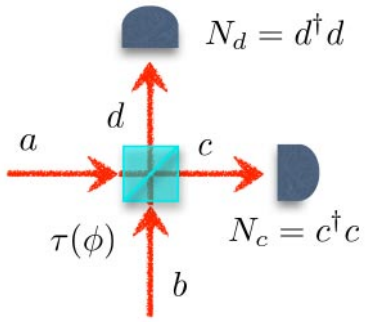

Fig. 3. – Simplified scheme of an interferometer equivalent to the Mach-Zehnder configuration in fig. 2. The measured phase shift ϕ can be summarised by the presence of a beam splitter transmissivity $\tau(\phi) = \cos^2(\phi/2)$. The two input bosonic field modes, a and b, evolve into the output filed modes c and d, that are finally detected by measuring the number of photons N_c and N_d, respectively.

and with the phase shift described in appendix A, the input field modes evolve into the output modes

$$c = \cos(\phi/2)\, a + \sin(\phi/2)\, b, \tag{10a}$$

$$d = \cos(\phi/2)\, b - \sin(\phi/2)\, a. \tag{10b}$$

The final stage of an interferometer is the photodetection of the beams leading to the measurement of the number of photons $N_c \equiv N_c(\phi)$ and $N_d \equiv N_d(\phi)$ and, finally, a suitable function $f(N_c, N_d)$ is evaluated (usually, as we will see later, the sum $N_c + N_d$ or the difference $N_c - N_d$ of the two quantities) obtaining a data sample. The outcomes x are distributed according to the probability distribution $p(x|\phi)$ which, of course, depends on the states of the optical input beams. The information about ϕ is retrieved using the estimator

$$\mathcal{O}(\phi) = \int_\Omega x\, p(x|\phi)\, \mathrm{d}x, \tag{11}$$

Ω being the data sample space, whereas the sensitivity $\mathcal{S}$ of the interferometer is given by the relation

$$\mathcal{S}(\phi) = \frac{\sqrt{\mathrm{var}[\mathcal{O}(\phi)]}}{|\partial_\phi \mathcal{O}(\phi)|}\,. \tag{12}$$

Whenever $p(x|\phi)$ can be approximated by a Gaussian distribution with standard deviation σ, it easy to show that [33]

$$\mathcal{S}(\phi) \approx \frac{1}{\sqrt{F(\phi)}} \approx \sigma, \tag{13}$$

where

$$F(\phi) = \int_\Omega p(x|\phi)\, [\partial_\phi \log p(x|\phi)]^2\, \mathrm{d}x \tag{14}$$

is the Fisher information introduced in sect. **2**.

In order to show how the presence of nonclassical states can improve the sensitivity, we first consider the scheme in fig. 3 when a coherent state $|\alpha\rangle_a$ and the vacuum state $|0\rangle_b$ enter the two ports of the interferometer. We recall that the coherent state represents, with good approximation, the output state of a laser with average number of photons given by $N = |\alpha|^2$ and standard deviation $|\alpha| = \sqrt{N}$ [34] (see appendix B for further details about coherent states).

If we assume to measure the photon number difference at the output, namely

$$\mathcal{O}(\phi) = D_-(\phi) \equiv \mathrm{Tr}[\varrho_{\mathrm{in}}(N_c - N_d)], \tag{15a}$$

$$= N_c(\phi) - N_d(\phi), \tag{15b}$$

with

$$\varrho_{\mathrm{in}} = |\alpha\rangle_a\langle\alpha| \otimes |0\rangle_b\langle 0|, \tag{16}$$

then we obtain the typical interference fringes, as reported in fig. 4(a). Since $D_-(\phi) = |\alpha|^2 \cos\phi$ and $\mathrm{var}[D_-(\phi)] = |\alpha|^2$, it is easy to show that the sensitivity of this interferometer is

$$\mathcal{S}_{\mathrm{cl}}(\phi) = \frac{1}{|\alpha|}\frac{1}{|\sin\phi|}\,, \tag{17}$$

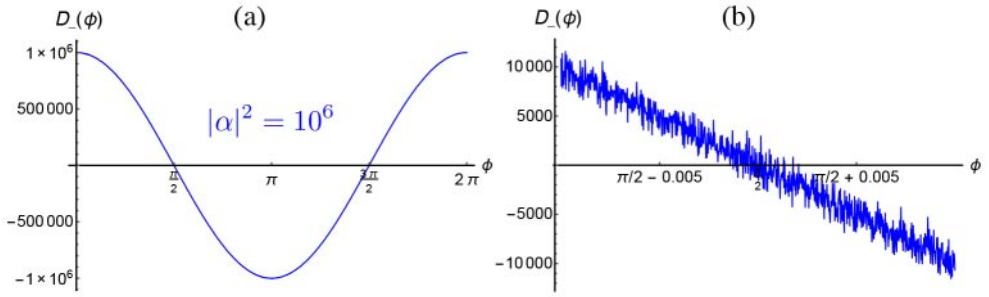

Fig. 4. – (a) Interference fringes (Monte Carlo simulated data). Typical plot of the photon number difference $D_-(\phi)$ as a function of ϕ at the output of an interferometer fed with a coherent state with amplitude $|\alpha|^2 = 10^6$ and the vacuum in the other input port. (b) Magnification of the region near $\phi = \pi/2$ of the previous plot: we can see the noise due to the photon number fluctuations.

(the subscript "cl" underlines the use of classical light, such as the coherent state) which reaches the minimum for $\phi = \phi_0 = \pi/2$. The value of the phase leading to the minimum sensitivity is usually called "working regime" of the interferometer: here a small change of the phase produces a large effect on the quantity $D_-(\phi)$, as we can see from fig. 4(b), since the absolute value of derivative at the denominator of eq. (12) reaches its maximum.

If we consider a scheme in which only one port of the interferometer is monitored, say the port corresponding to mode d, one finds analogous results, but now

$$\mathcal{O}(\phi) = N_d(\phi) \tag{18a}$$

$$= |\alpha|^2 \sin^2(\phi/2), \tag{18b}$$

and $\mathrm{var}[N_d(\phi)] = |\alpha|^2 \sin^2(\phi/2)$; therefore, the sensitivity becomes

$$\mathcal{S}_{\mathrm{cl}}(\phi) = \frac{1}{|\alpha|} \frac{1}{|\cos(\phi/2)|}\,. \tag{19}$$

Note that in this case the working regime is $\phi = 0$, corresponding to the so-called "dark port" as expected (we will briefly consider this configuration at the end of this section). This is the typical working regime of gravitational wave antennas [35]. In both the cases, however, the minimum sensitivity scales as $\propto N^{-1/2}$, N being the average number of photons circulating in the interferometer. This is the well-known *shot-noise scaling*. We will see that this limit can be beaten exploiting nonclassical optical states up to reaching the *Heisenberg scaling* $\propto N^{-1}$ [36-41].

In order to improve the sensitivity, we should look for a way to increase the value of the denominator of eq. (12) and/or to reduces the fluctuations of the measured quantity at the numerator. In this last case we can exploit the nonclassical properties of a particular class of states called squeezed states (see appendix C for some details about the definition and the main properties of squeezed states).

If we substitute to the vacuum a *squeezed* vacuum state, the two-mode input state reads

$$\varrho_{\mathrm{in}} = |\alpha\rangle_a\langle\alpha| \otimes |0, r\rangle_b\langle 0, r|, \tag{20}$$

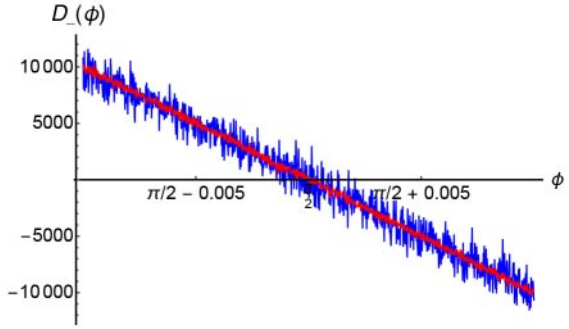

Fig. 5. – Same plot as in fig. 4(b) (blue line) and with a squeezed vacuum $|0, r\rangle$ instead of the vacuum, with number of squeezing photons $\lambda = \sinh^2 r = 4$, corresponding to about 12.5 dB, and the same coherent amplitude $|\alpha|^2 = 10^6$ (red line). Note that $\lambda \ll |\alpha|^2$. We can see that the photon number fluctuations are clearly reduced by the presence of squeezing.

where $|0, r\rangle_b$ is a squeezed state with 0 coherent amplitude and squeezing parameter r (see appendix C). The analytical formula of the sensitivity is now quite cumbersome [33] and is not reported explicitly. Nevertheless, fig. 5 shows the effects of the presence of squeezing, *i.e.* a noncalssical resource, on the interference fringes. Though the number of squeezed photon for the chosen parameters is extremely small with respect to number of coherent photons ($\lambda = \sinh^2 r = 4 \ll |\alpha|^2 = 10^6$), we can see a reduction of the photon number fluctuation which improves the sensitivity of the interferometer [38]. This is clear from fig. 6, where we plot the ratio

$$R_{\mathrm{sq/cl}} = \frac{\mathcal{S}_{\mathrm{sq}}(\phi)}{\mathcal{S}_{\mathrm{cl}}(\phi)} \tag{21}$$

between the sensitivity in the presence of squeezing ($\mathcal{S}_{\mathrm{sq}}$) and without it ($\mathcal{S}_{\mathrm{cl}}$) as a function of the measured phase ϕ. It is worth noting that only for $\phi \approx \pi/2$ the use of squeezing

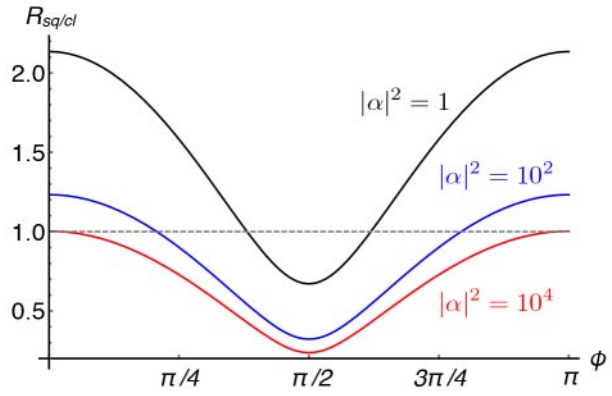

Fig. 6. – Plot of the ratio $R_{\mathrm{sq/cl}} = \mathcal{S}_{\mathrm{sq}}(\phi)/\mathcal{S}_{\mathrm{cl}}(\phi)$ between the sensitivity in the presence of squeezing ($\mathcal{S}_{\mathrm{sq}}$) and without it ($\mathcal{S}_{\mathrm{cl}}$) as a function of the measured phase ϕ. We used the same squeezing parameter as in fig. 5 and different values of $|\alpha|^2$. When $R_{\mathrm{sq/cl}} < 1$ squeezing turns out to be a useful resource for phase estimation.

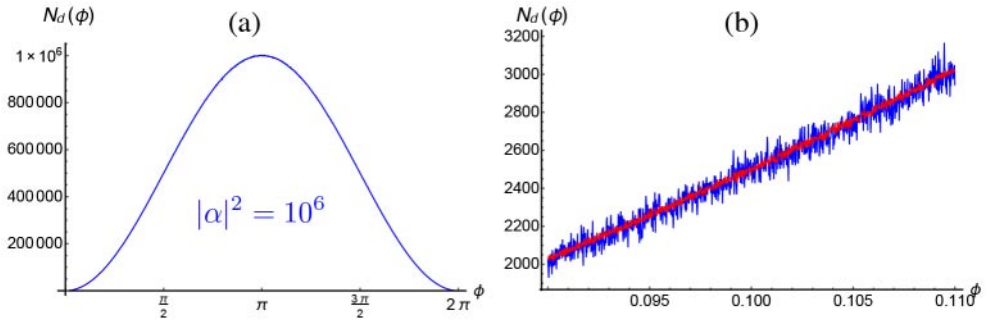

Fig. 7. – (a) Interference fringes (Monte Carlo simulated data) when only the port corresponding to mode d (see fig. 3) is monitored. Typical plot of the photon number $N_d(\phi)$ as a function of ϕ at the output of an interferometer fed with a coherent state with amplitude $|\alpha|^2 = 10^6$ and the vacuum in the other input port. (b) Magnification of the region approaching $\phi = 0$: we can see the noise due to the photon number fluctuations in the presence of coherent state and vacuum (blue line) and their reduction when the vacuum state is substituted with a squeezed vacuum (red lines).

leads to improved interferometer performances. This can be understood by inspecting the explicit expression of the variance of $D_-(\phi)$, which is now phase sensitive because of the presence of squeezing and reads

$$\text{(22)}\quad \mathrm{var}[D_-(\phi)] = |\alpha|^2 \left[1 - 2\sqrt{\lambda}\left(\sqrt{\lambda+1} - \sqrt{\lambda}\right)\sin^2\phi\right] + \lambda\left[1 + (1+2\lambda)\cos^2\phi\right].$$

Therefore, we have

$$\text{(23)}\qquad |\alpha|^2 \left[1 - 2\sqrt{\lambda}\left(\sqrt{\lambda+1} - \sqrt{\lambda}\right)\right] + \lambda \leq \mathrm{var}[D_-(\phi)] \leq |\alpha|^2 + 2\lambda(1+\lambda),$$

where the minimum is achieved for $\phi = \pi/2$ and the maximum for $\phi = 0, \pi$. For what concerns the expectation value of the photon number difference, the squeezing just affects the amplitude of the interference fringes, namely

$$\text{(24)}\qquad D_-(\phi) = \left(|\alpha|^2 - \lambda\right)\cos\phi.$$

Note that, in order to have $\mathrm{var}[D_-(\pi/2)] < |\alpha|^2$, we should require $\lambda < 4|\alpha|^2/(1+4|\alpha|^2)$, otherwise the squeezing resource becomes useless. Moreover, in the regime $\lambda \ll |\alpha|^2$ (see the lower red line in fig. 6) we find

$$\text{(25)}\qquad \mathrm{var}[D_-(\phi)] \approx |\alpha|^2 \left[1 - 2\sqrt{\lambda}\left(\sqrt{\lambda+1} - \sqrt{\lambda}\right)\sin^2\phi\right],$$

and we can see that it always beats the performance of an interferometer fed by the coherent state (and, of course, the vacuum).

For the sake of completeness in fig. 7(a) we report the interference fringes when only one port of the interferometer is monitored and the number of photons $N_d(\phi)$ is recorded. In this case, as we noted above, the working regime is $\phi = 0$, where the intensity fluctuations, which depends on the coherent state amplitude (see appendix B), vanishes,

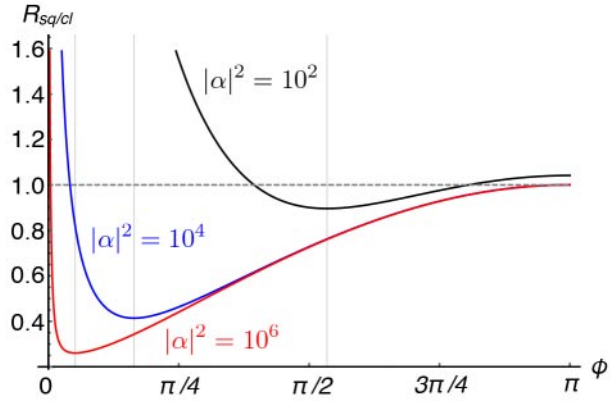

Fig. 8. – Plot of the ratio $R_{\mathrm{sq/cl}} = \mathcal{S}_{\mathrm{sq}}(\phi)/\mathcal{S}_{\mathrm{cl}}(\phi)$ between the sensitivity in the presence of squeezing ($\mathcal{S}_{\mathrm{sq}}$) and without it ($\mathcal{S}_{\mathrm{cl}}$) as a function of the measured phase ϕ when only the port of mode d (see fig. 3) is monitored. We used the same squeezing parameter as in fig. 5 and different values of $|\alpha|^2$. When $R_{\mathrm{sq/cl}} < 1$ squeezing turns out to be a useful resource for phase estimation. Note the presence of the minimum approaching $\phi = 0$ as the coherent state amplitude increases.

since the detected intensity is null. In fig. 7(b), blue line, we show the magnification of the region for ϕ approaching zero. As in the case of the measurement of $D_-(\phi)$, also in this one the presence of squeezing can help: the red line in fig. 7(b) is obtained by substituting to the vacuum a squeezed state with the same squeezing parameter used in fig. 5.

If we now consider the corresponding ratio $R_{\mathrm{sq/cl}}$ between the sensitivity in the presence of squeezing and without it reported in fig. 8, we can see that the minimum is not achieved in the working regime $\phi = 0$, but for a value that approaches it as the intensity of the coherent state increases. On the contrary, we recall that when the photocurrent difference $D_-(\phi)$ at the output is used to retrieve the information about the phase, the working regime at $\phi = \pi/2$ coincides with the optimal phase to fully exploit the squeezing resource, as we can see from fig. 5 and fig. 6.

Also in this case there are regions of the phase for which squeezing does not improve the performance of the interferometer. However, the analysis of the effect is more subtle than the previous case. In fact, while the mean value reads

$$N_d(\phi) = |\alpha|^2 \sin^2(2\phi) + \lambda \cos^2(2\phi), \tag{26}$$

the variance is now given by

$$\begin{aligned} \mathrm{var}[N_d(\phi)] = \frac{|\alpha|^2}{2}\left[1 - \cos\phi + \sqrt{\lambda}\left(\sqrt{\lambda+1} - \sqrt{\lambda}\right)\sin^2\phi\right] \\ + \frac{\lambda}{2}\cos^2\left(\frac{\phi}{2}\right)\left[2 + (1+2\lambda)(1+\cos\phi)\right], \end{aligned} \tag{27}$$

which depends on ϕ also in the absence of squeezing. If we focus on the working regime $\phi = 0$, we have $\mathrm{var}[N_d(0)] = 2\lambda(1+\lambda)$, which vanishes only for $\lambda = 0$, *i.e.* when the squeezed state is replaced by the vacuum. Nevertheless, squeezing can help in realistic

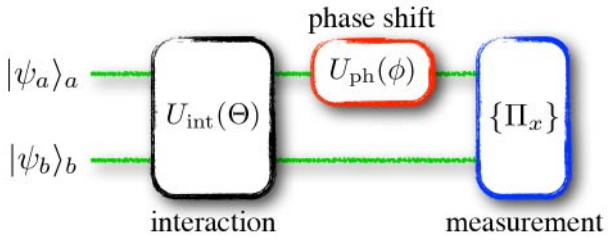

Fig. 9. – Diagram of an interferometer showing the main elements: the unitary interaction $U_{\rm int}(\Theta)$, the phase shift $U_{\rm ph}(\phi)$ and the measurement described by the POVM $\{\Pi_x\}$.

scenarios, in which one cannot set precisely the phase $\phi = 0$ because of the unavoidable experimental errors. As shown in fig. 8 (see the red curve for $|\alpha|^2 = 10^6$) a small deviation from $\phi = 0$ is enough to make the squeezing a useful resource. In fact, when a very large number of photons circulates in the interferometer, a phase shift slightly different from 0 is enough to bring a considerable number of photons to the detector. In this case the presence of squeezing can reduce the intensity fluctuation and, in turn, increase the sensitivity.

In the next section, we will investigate the limits imposed by quantum mechanics to the precision of optical interferometers by using the tools of quantum estimation theory introduced in sect. **2**. Moreover, we will also consider more general setups involving active devices, such as optical parametric amplifiers.

4. – Bounds to precision for quantum interferometry

When a particular measurement stage is chosen and the input states are given, in order to find the optimal working regime of an interferometer we should maximise the Fisher information with respect to all the involved parameters (characterising both the input states and the interferometer). Moreover, we should address and optimise the quantum Fisher information [20, 21] to study the ultimate bounds imposed by quantum mechanics, and find the optimal measurement to perform. To this aim it is useful to describe the interferometers as sketched in fig. 9. Here, the two modes of an input state

$$|\Psi\rangle\rangle = |\psi_a\rangle_a|\psi_b\rangle_b \tag{28}$$

interact through the unitary interaction $U_{\rm int}(\Theta)$, Θ representing the parameter of the interaction (such as the beam splitter transmissivity), then one of the modes undergoes a phase shift $U_{\rm ph}(\phi)$; finally, they are measured according to the POVM $\{\Pi_x\}$, x being the outcome of the measurement [18].

In general, different quantum optical states can be used to improve the sensitivity of an interferometer [5, 42, 43]. In this section we consider the class Gaussian states, namely, states described by Gaussian Wigner function which can be generated and manipulated with the current technology [44-46]. Therefore we can assume that the input states are two displaced squeezed states, *i.e.* $|\alpha, r\rangle|\gamma, \xi\rangle$ (for the sake of simplicity we drop the subscripts), where we can also assume $\alpha, \gamma, r, \xi \in \mathbb{R}$ [33]. In order to make the analysis

easier, it is useful to introduce the following relevant quantities:

$$N_{\rm tot} = \alpha^2 + \gamma^2 + \sinh^2 r + \sinh^2 \xi \quad \text{(total number of photons)},$$

$$\Delta = \frac{\alpha^2}{\alpha^2 + \gamma^2} \quad \text{(signal fraction)},$$

$$\beta_{\rm tot} = \frac{\sinh^2 r + \sinh^2 \xi}{N_{\rm tot}} \quad \text{(total squeezing fraction)},$$

$$\beta = \frac{\sinh^2 \xi}{N_{\rm tot}} \quad \text{(partial squeezing fraction)}.$$

As we discussed in sect. **2**, the inverse of the Fisher information sets a lower bound for the variance in estimating ϕ, known as Cramér-Rao bound, that is based on $p(x|\phi)$ and, thus, depends on the particular measurement we perform. It is possible, however, to find a measurable observable (an optimal POVM) that maximises the Fisher information [18, 19, 22]. This leads to an upper bound for the Fisher information, the *quantum Fisher information* (see sect. **2**).

In order to find the optimal POVM, one starts from the Born rule

$$p(x|\phi) = {\rm Tr}[\varrho_\phi \Pi_x], \tag{29}$$

where

$$\varrho_\phi = U_{\rm ph}(\phi) U_{\rm int}(\Theta) \varrho_{\rm in} U^\dagger_{\rm int}(\Theta) U^\dagger_{\rm ph}(\phi), \tag{30}$$

and $\varrho_{\rm in} = |\Psi\rangle\rangle\langle\langle\Psi|$. To find the optimal $\{\Pi_x\}$ we write the Fisher information as in eq. (4) and the corresponding quantum Fisher information $H(\phi)$ is such that $H(\phi) \geq F(\phi)$. Here we are not interested in the actual form of the POVM, but we will focus on the quantum Fisher information.

First of all we consider a passive interaction, namely, an interaction which does not change the energy of the input states. In particular, we assume that $U_{\rm int}(\Theta)$ describes the action of a balanced beam splitter (see appendix A)

$$U_{\rm int}(\Theta) \equiv \exp\left[\frac{\pi}{4}\left(a^\dagger b - a b^\dagger\right)\right], \tag{31}$$

where a and b are the boson field operators describing the two input modes. The maximisation of the Fisher information over all the involved quantities introduced above shows that the best configuration requires $\alpha = \gamma$ and $\xi = r$, corresponding to the following quantum Fisher information (the reader can find the details in ref. [37]), which depends only on $N_{\rm tot} = 2(\alpha^2 + \sinh^2 r)$ and $\beta_{\rm tot} = 2\sinh^2 r / N_{\rm tot}$:

$$\begin{aligned} &H_{\rm max}(N_{\rm tot}, \beta_{\rm tot}) = \\ &2N_{\rm tot}\left[2N_{\rm tot}\beta_{\rm tot}(2-\beta_{\rm tot}) + 2(1-\beta_{\rm tot})\sqrt{N_{\rm tot}\beta_{\rm tot}(2+N_{\rm tot}\beta_{\rm tot})}\right]. \end{aligned} \tag{32}$$

We can perform a further (numerical) maximisation of $H_{\rm max}(N_{\rm tot}, \beta_{\rm tot})$ with respect to the total squeezing fraction $\beta_{\rm tot}$. The results are shown in fig. 10(a), where we plot

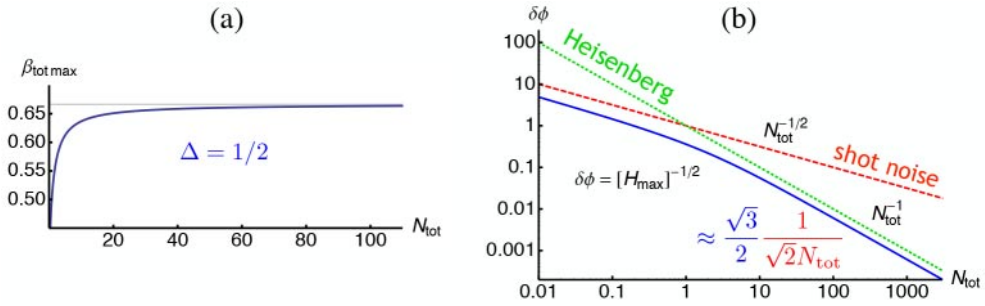

Fig. 10. – (a) Plot of the optimal value of β_{tot} maximising the quantum Fisher information (32) as a function of N_{tot}. As N_{tot} increases $\beta_{\mathrm{tot\,max}} \to 2/3$. (b) The phase sensitivity $\delta\phi = [H_{\mathrm{max}}]^{-1/2}$ as a function of N_{tot} (blue solid line), where we used the optimal value $\beta_{\mathrm{tot\,max}}$ given in panel (a). In the limit $N_{\mathrm{tot}} \gg 1$ we have $H_{\mathrm{max}} \approx \frac{8}{3}N_{\mathrm{tot}}^2$, that is the Heisenberg scaling. We also plot the shot-noise limit $N_{\mathrm{tot}}^{-1/2}$ (red dashed line) and the Heisenberg limit N_{tot}^{-1} (green dotted line).

$\beta_{\mathrm{tot\,max}}$ as a function of N_{tot}, whereas in fig. 10(b) we plot the corresponding phase sensitivity $\delta\phi = 1/\sqrt{H_{\mathrm{max}}}$ obtained by using the optimal squeezing fraction $\beta_{\mathrm{tot\,max}}$: it is clear that in the large energy regime ($N_{\mathrm{tot}} \gg 1$) the Heisenberg scaling is reached.

It is worth noting that the maximisation over all the parameters leads to the optimal symmetric input state $|\alpha, r\rangle|\alpha, r\rangle$. If we assume, however, that the input state has the form $|\alpha, 0\rangle|0, \xi\rangle$ (coherent state + squeezed vacuum [35]), the optimisation still gives the Heisenberg scaling for $N_{\mathrm{tot}} \gg 1$ but now $H_{\mathrm{max}} \approx 2N_{\mathrm{tot}}$, that is a slightly worse result than the one we obtained by considering displaced squeezed states.

Let's suppose, now, that the initial interaction is an active one, namely it increases the energy of the input states. A typical interaction of this kind is implemented by an optical parametric amplifier (OPA) [47] and it is the so-called two-mode squeezing interaction (see appendix D), described by the unitary operator:

$$U_{\mathrm{int}}(\Theta) \equiv \exp(\xi a^\dagger b^\dagger - \xi^* ab). \tag{33}$$

This operator, when applied to the vacuum state, generates the two-mode squeezed vacuum or twin-beam state, as explicitly shown in appendix D, namely:

$$|\mathrm{TWB}\rangle\rangle = \sqrt{1 - |\lambda|^2} \sum_n \lambda^n |n\rangle_a |n\rangle_b, \tag{34}$$

with $\lambda = e^{\arg[\xi]} \tanh|\xi|$, that is a continuous-variable entangled state whose nonclassical features are exploited in many continuous-variable quantum information processing protocols [10].

This kind of interferometer is also referred to as *coherent light boosted interferometer* (CLBI) [48, 49]. Since the interaction imposes phase-sensitive amplification (*i.e.* two-mode squeezing) introducing quantum correlations between the two modes, we can choose as inputs two classical signals, namely, a couple of coherent states $|\alpha\rangle_a|\gamma\rangle_b$, $\alpha, \gamma \in \mathbb{R}$.

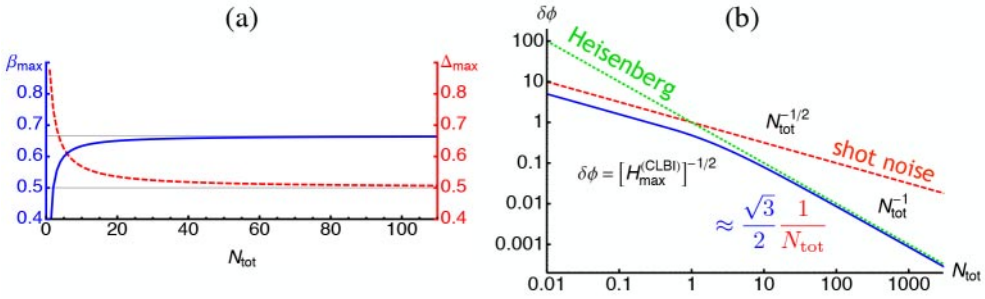

Fig. 11. – (a) Plot of $\beta_{\max}$ (blue sold line) and $\Delta_{\max}$ (red dashed line) maximising the quantum Fisher information in the case of the CLBI as function $N_{\rm tot}$. In the limit $N_{\rm tot} \gg 1$ we have $\beta_{\max} \to 2/3$ and $\Delta_{\max} \to 1/2$. (b) The corresponding phase sensitivity $\delta\phi = [H_{\max}^{(\rm CLBI)}]^{-1/2}$ as a function of $N_{\rm tot}$ (blue solid line). In the limit $N_{\rm tot} \gg 1$ we have $H_{\max} \approx \frac{4}{3}N_{\rm tot}^2$, that is the Heisenberg scaling. We also plot the shot-noise limit $N_{\rm tot}^{-1/2}$ (red dashed line) and the Heisenberg limit $N_{\rm tot}^{-1}$ (green dotted line).

Now the relevant quantities are

$$N_{\rm tot} = (\alpha^2 + \gamma^2 + 1)\cosh(2r) + 2\alpha\gamma\cos(\theta)\sinh(2r) - 1 \quad \text{(total number of photons)},$$
$$\Delta = \frac{\alpha^2}{\alpha^2 + \gamma^2} \quad \text{(signal fraction)},$$
$$\beta = \frac{\sinh^2 \xi}{N_{\rm tot}} \quad \text{(total squeezing fraction)}.$$

Proceeding as in the case of the passive interferometer, we can maximise the quantum Fisher information with respect to β and Δ for fixed energy $N_{\rm tot}$. In fig. 11(a) we plot the signal fraction $\Delta_{\max}$ and the squeezing fraction $\beta_{\max}$ giving the maximal quantum Fisher information $H_{\max}^{(\rm CLBI)}$ plotted in fig. 11(b). By comparison between fig. 10(b) and fig. 11(b) in the large energy regime we can see that the passive interferometer outperforms the active one. Nevertheless, in the presence of losses and realistic measurement the latter turns out to be useful, as we are going to show in the following.

A thorough analysis of passive and active interferometers using passive and active detection stage can be found in ref. [33], while here we summarise the main results we obtained also in the presence of non-unit quantum detection efficiency (in appendix E we describe the model used to include the quantum efficiency in our analysis). As a matter of fact, one can choose any possible combination of active/passive interaction and active/passive detection.

We first consider the most common configuration, in which a balanced, 50:50, beam splitter is used in the initial interaction and before photodetection, as shown in the scheme in fig. 12: the measured quantity is the difference $D_-(\phi)$ and the sensitivity is given by

$$\mathcal{S}_1(\phi) = \frac{\sqrt{\mathrm{var}[D_-(\phi)]}}{|\partial_\phi D_-(\phi)|}, \tag{35}$$

In fig. 12(a) we plot the sensitivity of the interferometer as a function of $N_{\rm tot}$ after the

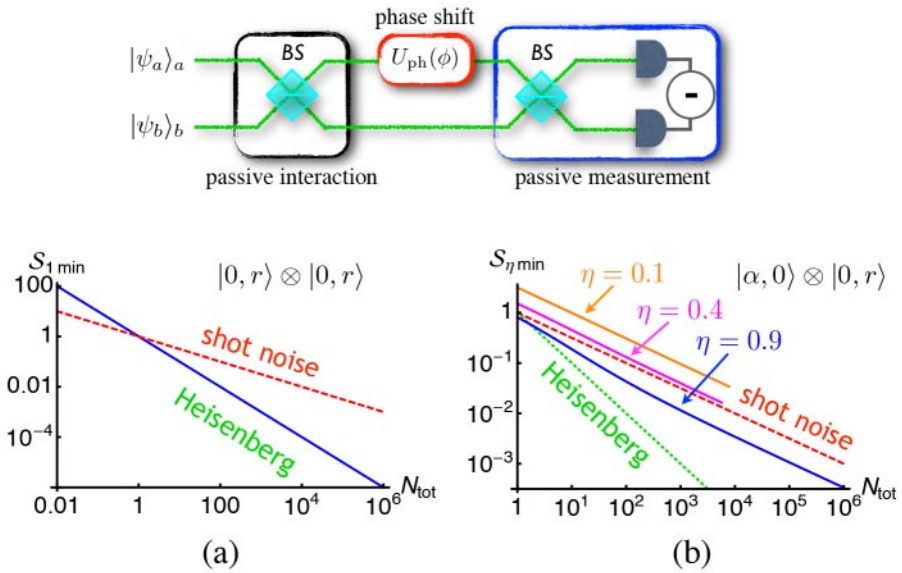

Fig. 12. – Interferometer with passive interaction and passive detection scheme: the two input states are mixed at a balanced beam splitter (BS) before the phase shift and interfere again at another BS before the photodetection. Here one evaluates the difference $D_-(\phi) = N_1(\phi) - N_2(\phi)$ between the detected photons in order to retrieve the information about ϕ. (a) Minimised sensitivity of the interferometer for unit quantum efficiency η as a function of $N_{\rm tot}$. The optimal input states are two squeezed vacua. (b) Minimised sensitivity of the interferometer for different values η. Now the optimal input states are a coherent state and a squeezed vacuum (see ref. [33] for further details). The shot-noise and the Heisenberg scalings are also reported for comparisons.

optimisation (*i.e.* the minimisation of the sensitivity) with respect to the input states. In the presence of unit quantum efficiency, we find that the optimal input states are a couple of squeezed vacuum states: this choice allows us to obtain the Heisenberg scaling. However, as one may expect, when $\eta < 1$ we can only achieve the shot-noise limit [50] and, in this case, the optimal input states are a coherent state and the squeezed vacuum (see ref. [33] for further details) as reported in fig. 12(b).

As we have seen, in the presence of losses (*i.e.* $\eta < 1$) the Heisenberg scaling is no longer achievable by the passive-passive configuration. Nevertheless, if we substitute to the second beam splitter an OPA (characterised by the squeezing parameter r_1), thus we are using an active detection stage, we can face the losses. Moreover, upon a suitable optimisation with respect to the squeezing parameter r_1 we can still obtain the Heisenberg scaling. This scenario is shown in fig. 13. We note that the use of an active detection stage based on an OPA requires to measure the sum

$$D_+(\phi) \equiv \mathrm{Tr}[\varrho_{\rm in}(N_c + N_d)], \tag{36a}$$

$$= N_1(\phi) + N_2(\phi), \tag{36b}$$

since the difference is now independent of ϕ, as the reader can easily verify. Therefore,

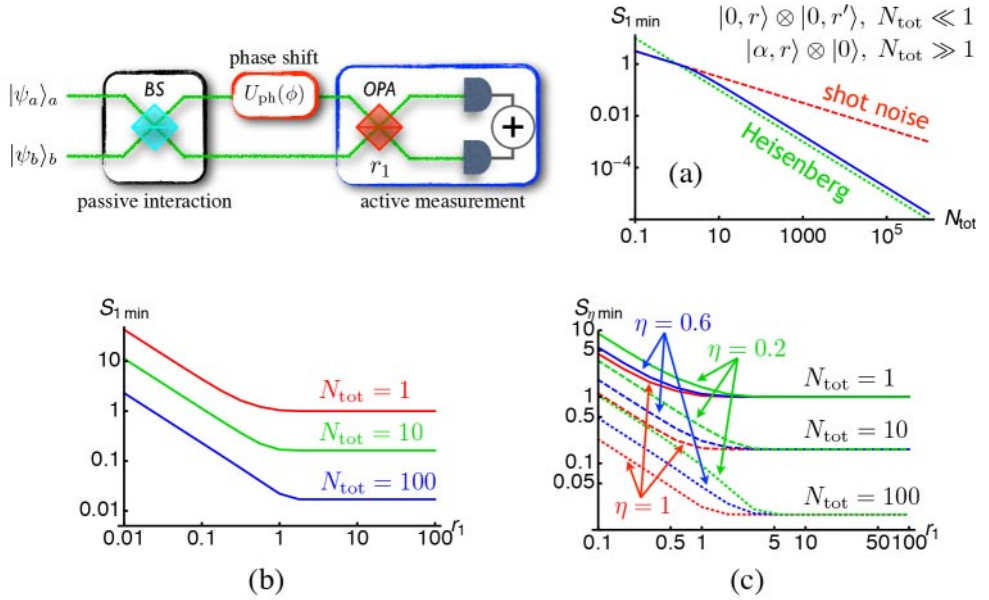

Fig. 13. – Interferometer with passive interaction and active detection stage: the two input states are mixed at a balanced beam splitter (BS) before the phase shift and, then, they undergo a two-mode squeezing interaction through an OPA before the photodetection. Here one evaluates the sum $D_+(\phi) = N_1(\phi) + N_2(\phi)$ between the detected photons in order to retrieve the information about ϕ. (a) Minimised sensitivity $\mathcal{S}_{1\,\rm min}$ of the interferometer a function of $N_{\rm tot}$. The optimal input states are two squeezed vacua with different energy (for $N_{\rm tot} \ll 1$) or a squeezed coherent state and the vacuum (for $N_{\rm tot} \gg 1$). The shot-noise and the Heisenberg scalings are also reported for comparisons. (b) Minimised sensitivity $\mathcal{S}_{\eta\,\rm min}$ as a function of r_1 for different values of $N_{\rm tot}$. (c) Minimised sensitivity $\mathcal{S}_{\eta\,\rm min}$ as a function of r_1 for different values of $N_{\rm tot}$ and η. We can see that, as r_1 increases, $\mathcal{S}_{\eta\,\rm min}$ becomes independent of η and depends only on the total energy $N_{\rm tot}$.

the sensitivity is defined as

$$\mathcal{S}_1(\phi) = \frac{\sqrt{\mathrm{var}[D_+(\phi)]}}{|\partial_\phi D_+(\phi)|}\,. \tag{37}$$

Assuming $\eta = 1$, the optimisation shows that we identify two regimes: for low energy ($N_{\rm tot} \ll 1$) the optimal input state is a couple of squeezed states with different energy, but here we can reach only the shot-noise scaling; for $N_{\rm tot} \gg 1$, however, the use of a squeezed coherent state together with the vacuum allows to reach the Heisenberg scaling, namely (details can be found in ref. [33])

$$\mathcal{S}_{1\,\rm min} \approx \frac{1+\sqrt{2}}{\sqrt{2}N_{\rm tot}}\,. \tag{38}$$

The result is shown in fig. 13(a). In fig. 13(b) we plot $\mathcal{S}_{1\,\rm min}$ as a function of r_1. As we have mentioned above, the use of an active detection can fight the detrimental effects of losses (*i.e.* non-unit quantum efficiency) on the sensitivity. This can be seen analysing

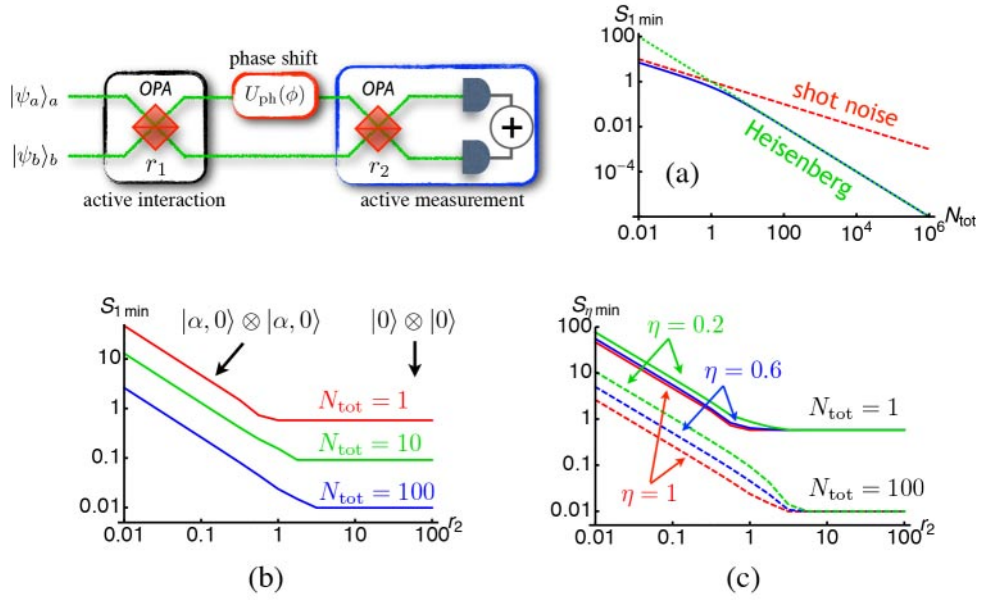

Fig. 14. – Interferometer with active interaction and detection stage: the two input states interact at a first OPA before the phase shift and, then, they undergo another two-mode squeezing interaction through a second OPA before the photodetection. The sum $D_+(\phi) = N_1(\phi) + N_2(\phi)$ between the detected photons is then evaluated in order to retrieve the information about ϕ. (a) Minimised sensitivity $\mathcal{S}_{1\,\rm min}$ of the interferometer a function of $N_{\rm tot}$. The shot-noise and the Heisenberg scalings are also reported for comparisons. (b) Minimised sensitivity $\mathcal{S}_{\eta\,\rm min}$ as a function of r_2 for different values of $N_{\rm tot}$ (we recall that we have performed the optimisation over all the other involved parameters [33]). The optimal input states are two coherent states (for $r_2 \ll 1$) or the vacuum (for $r_2 \gg 1$). (c) Minimised sensitivity $\mathcal{S}_{\eta\,\rm min}$ as a function of r_2 for different values of $N_{\rm tot}$ and η. We can see that, as r_2 increases, $\mathcal{S}_{\eta\,\rm min}$ becomes independent of η and depends only on the total energy $N_{\rm tot}$.

fig. 13(c): here we plot $\mathcal{S}_{\eta\,\rm min}$ as a function of r_1 for different values of the quantum efficiency η and $N_{\rm tot}$. It is clear that, after the optimisation, as r_1 increases we have

$$\mathcal{S}_{\eta\,\rm min} \to \mathcal{S}_{1\,\rm min}, \tag{39}$$

that is the Heisenberg scaling is restored.

We now turn our attention to active interferometers, in which the first beam splitter of the passive ones is substituted with an OPA with squeezing parameter r_1. The study of this kind of interferometers shows that the use of a passive detection stage does not allow to go beyond the shot-noise limit, also in the lossless case [33]. Therefore, here we consider only the configuration with an active detection stage characterised by an OPA with squeezing parameter r_2 (see the scheme in fig. 14). Moreover, the numerical analysis proves that the sensitivity is minimised for $r_2 \gg 1$ [33], thus we consider this regime. The result for $\eta = 1$ is reported in fig. 14(a), where we report $\mathcal{S}_{1\,\rm min}$ as a function of $N_{\rm tot}$: also in this case the Heisenberg scaling is achieved as the energy increases. Figure 14(b) shows $\mathcal{S}_{1\,\rm min}$ as a function of r_2: it is clear that the minimum of the sensitivity is obtained when the OPA employed at the detection introduces a large number of photons ($r_2 \gg 1$),

as mentioned above. It is interesting to note that the optimal input states depend on the energy added by the active detection stage: if $r_2 \ll 1$ then we should use two coherent states with the same energy, whereas for $r_2 \gg 1$ the best choice is the vacuum state.

Finally, as in the passive/active interferometer, in fig. 14(c) we plot $\mathcal{S}_{\eta\,\min}$ as a function of r_2 and different values of $N_{\rm tot}$ and η: the use of an active detection stage allows to reach the Heisenberg scaling of the lossless case also in the presence of non-unit quantum efficiency, namely (see ref. [33])

$$\mathcal{S}_{1\,\min} \approx \frac{1}{\sqrt{N_{\rm tot}(N_{\rm tot}+2)}}\,, \tag{40}$$

for the large energy regime $N_{\rm tot} \gg 1$.

5. – Practical quantum illumination

In sects. **3** and **4** we have seen that the quantum properties of light, such as "squeezing", can be a useful resource to enhance the sensitivity of interferometers going beyond the quantum shot-noise limit and finding applications in gravitational wave antennas [35, 36].

Here we focus on the use of quantum correlation and, in particular, the entanglement existing between two beams of light generated by an OPA, the so-called twin beams (see appendix D), in order to detect the presence of an opaque object in a very noisy background.

We will describe the object as a beam splitter embedded in a background of "thermal" radiation: the problem is then to distinguish the photons scattered by the object from those belonging to the background, when the latter is predominant. This scheme is known as *quantum illumination* [51, 52]. From the theoretical point of view, one can find an optimal strategy based on twin beams which outperforms any classical one [52, 53]. However, this kind of receivers turns out to be very challenging from the experimental point of view [53, 54].

In the following we show the main results one can obtain using a quantum illumination protocol based on current technology [55, 56] which performs astonishingly better than a classical one based on classically correlated light [57]. As a matter of fact, this protocol cannot aim to achieve the optimal target-detection bounds of ref. [52], but it exhibits very large quantum enhancement and robustness against noise as in the case of the original idea.

In fig. 15 we report a pictorial view of the experimental schemes used to implement the quantum illumination protocol and the classical counterpart. The twin beams are generated by a beta-barium borate crystal (BBO) with an average number of photons per spatio-temporal mode $\mu = 0.075$. They are then addressed to a high quantum efficiency CCD camera, able to measure the correlations between the two beams.

In the quantum illumination protocol, see fig. 15(a), an object, a 50:50 beam splitter, intercepts one of the two correlated beams and superimposes to it a thermal background produced by scattering a laser beam on an Arecchi's rotating ground glass. We assume that the background is caracterised by an average number of photons N_b distributed among M_b modes. The other beam is instead directly detected. When the beam splitter is removed, only the background reaches the detector.

In the classical illumination protocol, reported in fig. 15(b), we should substitute to the twin beams two classical correlated beams. These latter are obtained by splitting

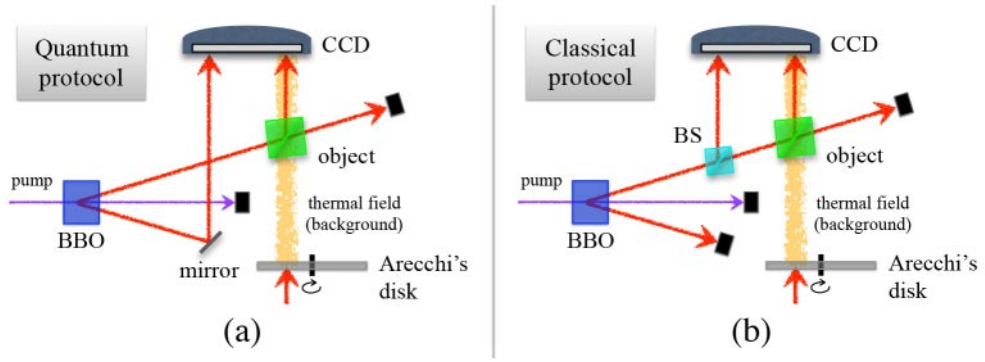

Fig. 15. – Schematic view of the quantum illumination protocol. (a) Quantum illumination protocol: one of the two beams of a twin-beam state generated by a BBO is reflected toward the detection system. If the beam splitter (the object) is present, the correlated beam is partially detected by means of a CCD camera, together with the thermal field from Arecchi's disk; otherwise it is lost. (b) Classical illumination protocol: now one beam of the twin beams is stopped and the other one is split at a beam splitter (BS) for generating correlated multithermal beams. The pump power is adjusted in order to obtain the same energy as in the case (a). Further details about the experimental setup can be found in ref. [57].

a single beam from the BBO but adjusting the pump power in order to have the same intensity, time and spatial coherence properties as in the quantum case [57]. As shown in appendix D, the single beam of a twin beam corresponds to a thermal state: when the thermal state is split at a beam splitter the two emerging beams are classically correlated.

Whereas the reader can find a thorough and detailed analysis of the source of the quantum enhancement in refs. [57,58] and [59], here we only report the results about the error probability in the discrimination of the presence from the absence of the object. The figure of merit we used in our experiment is the correlation in the photon numbers N_1 and N_2 detected by pairs of pixels of the CCD intercepting correlated modes of beams $a_1$and a_2, respectively. In particular we focus on the covariance

$$\Delta_{1,2} = \langle N_1 N_2 \rangle - \langle N_1 \rangle \langle N_2 \rangle, \tag{41}$$

where $\langle \cdots \rangle$ is the average over the set of a given number of realisations (since the experiment uses a CCD camera, the number of realisations is the number of correlated pixels pairs) [57] and $N_k = a_k^\dagger a_k$, $k = 1, 2$.

The problem of discriminating the presence from the absence of the object is then equivalent to that of distinguishing between two corresponding values of $\Delta_{1,2}$. More precisely, we can choose a threshold value of $\Delta_{1,2}$ above which we can infer that the object is present otherwise it is not. Typical results are shown in fig. 16, where the measured values of the covariance and their error bars are plotted as a function of the background photons N_b for the quantum illumination (left panel) and classical illumination (right panel): note how the quantum protocol outperforms the classical one.

Since the experimental values unavoidably fluctuate, we have to evaluate the error probability P_{err} of the discrimination, that is the probability to infer the wrong answer given a value of the covariance. If we know only the mean value and the variance of a certain quantity, we should assign a Gaussian probability distribution to that quantity

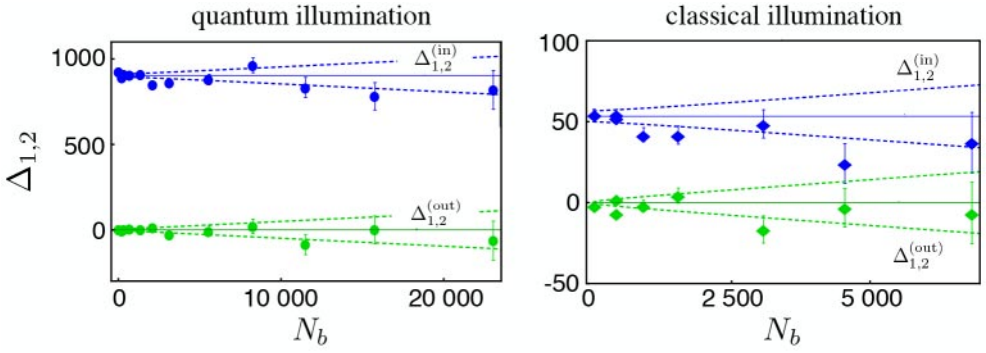

Fig. 16. – Typical plot of the covariance in the presence, $\Delta_{1,2}^{(\mathrm{in})}$ (blue), and in the absence, $\Delta_{1,2}^{(\mathrm{out})}$ (green), of the object as a function of the average number of background photons N_b distributed among $M_b = 1300$ modes. The plot on the left refers to the quantum illumination protocol, whereas the one on the right to the classical counterpart as described in the text. The bars are the effect of the background noise on the covariance estimation. We also report the expectations (horizontal lines) and the corresponding uncertainty interval as calculated theoretically. It is clear that the presence or the absence of the object can be inferred by addressing the value of the covariance. Notice the enhancement due to the quantum protocol. Data comes from ref. [57].

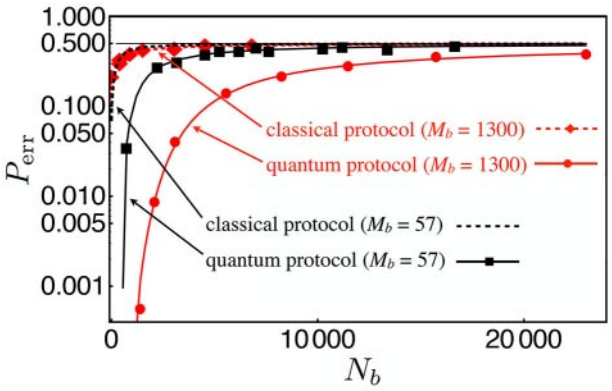

Fig. 17. – Plot of the target detection error probability as a function of the background photons N_b and for two values of the number of modes, $M_b = 57$ (black) and $M_b = 1300$ (red). The symbols refer to the experimental data whereas the lines are the theoretical previsions. The points corresponding to $M_b = 1300$ have been obtained by processing the data in fig. 16 as described in the text.

according to the maximum entropy principle (see, for instance, ref. [60]). Therefore it is possible to associate a probability distribution with each point of fig. 16 and we can evaluate the error probability by fixing a threshold value of the covariance chosen in order to minimise P_{err}. In fig. 17 we show P_{err} as a function of N_b for two values of the number of background modes M_b, in the case of both the quantum illumination protocol and the classical one. We can also see that the quantum improvement becomes larger as M_b increases. In particular, the points corresponding to $M_b = 1300$ have been obtained by processing the data in fig. 16 as described above.

Entanglement is usually a fragile resource which should be carefully protected by the environment and, thus, the advantages of entangled and quantum states can be exploited only in advanced quantum laboratories or for academic discussions. Nevertheless, the results we presented in this section show that it is possible to obtain orders of magnitude improvements compared to the classical protocol, independent of the amount of noise and losses, by using devices available nowadays. Therefore, this kind of "practical" quantum illumination protocol based on photon counting can have interesting potentialities to promote the usage of quantum correlated light in real and more complex scenarios [61,62].

6. – Beyond single-interferometer setups

In sect. **4** we have seen how quantum light can be exploited in interferometers to improve the estimation of an unknown phase shift also beating the shot-noise limit and, thus, opening the way to a new generation of quantum-enhanced interferometers [35]. However, as illustrated in sect. **5**, quantum correlations between light beams can be used to successfully outperform the performance of standard imaging protocols. The question that now arises is whether it is possible to exploit quantum correlations to further improve interferometers. In fact, recently quantum correlations have received a lot of attention as a key ingredient in advanced quantum metrology protocols [63, 64].

In the following section we will review the main theoretical results we obtained coupling two interferometers via quantum-correlated beams. In particular, we show how protocols based on quantum-correlated interferometers lead to substantial advantages with respect to the use of classical light, up to a noise-free scenario for the ideal lossless case [65, 66] also in the presence of some additional noise [67].

7. – Probing the noncommutativity of position and momentum

One of the most interesting applications of interference devices concerns the quantum gravity tests. The noncommutativity at the Planck scale ($l_p = 1.616 \times 10^{-35}\,\mathrm{m}$) of position variables in different directions gives rise to quantum fluctuations of the space geometry [68, 69] which, under particular conditions, could lead to detectable effects in cavities with microresonators [70] or in two coupled interferometers, the so-called holometer [71, 72]. In the latter case, the predicted noncommutativity leads to an additional phase noise, the "holographic noise".

If we consider a single interferometer based on a single beam splitter, such as the Michelson interferometer sketched in fig. 18, in the presence of the holographic noise the jitter in the beam splitter position leads to fluctuations of the measured phase. Since, the phase shift can be seen as a measurement of the beam splitter position, the phase fluctuations are directly related to the fluctuations $\Delta x_k^2 = l_p\, L$ of the coordinate x_k, $k = 1, 2, 3$, L being the length of the interferometer's arm (for the sake of clarity we recall that $L = 600\,\mathrm{m}$ for GEO600 and $L = 4\,\mathrm{km}$ for LIGO) [71]. Therefore, the holographic noise accumulates as a random walk and becomes detectable.

Unfortunately, the most precise interferometers able to detect gravitational waves have a resolution at low frequencies $f \ll c/(4\pi L)$ not enough to detect the holographic noise (the interested reader can find plenty of details about the holographic noise and its origin in ref. [71]). Nevertheless, it could be possible to identify this noise by evaluating the cross-correlation between the two equal interferometers of the holometer when placed in the same space-time volume: while the shot noises of the interferometers are uncorrelated and do vanish over a long integration time, the holographic noises are not. Moreover, one

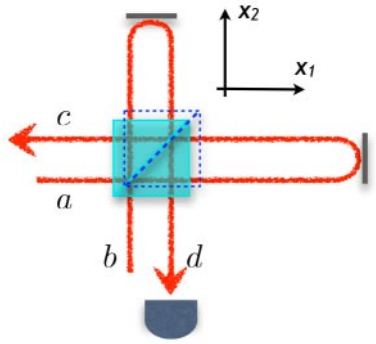

Fig. 18. – The jitter in the beam splitter position (x_1, x_2) leads to fluctuations in the measured phase. See the text for details.

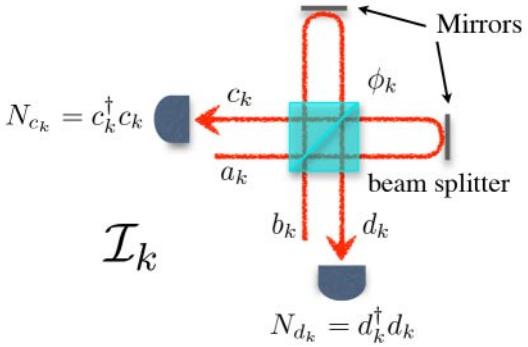

Fig. 19. – Scheme of the Michelson interferometer $\mathcal{I}_k$, $k = 1, 2$. We reported the involved modes and the measured quantities.

can also "turn off" the holographic fluctuations by separating the space-time volumes, thus obtaining a background estimation. As a matter of fact, the ultimate limit for the holometer sensibility is related to the shot noise. In the following we will discuss how it could be possible to go beyond this limit by using the quantum optical states we introduced in sect. **4** in the case of a single interferometer. We consider two Michelson interferometers $\mathcal{I}_k$, $k = 1, 2$, as shown in fig. 19, where we reported the involved modes and the measured number operators at the outputs. The k-th interferometer detects the phase shift ϕ_k. We are interested in a joint measurement, thus we should consider a suitable operator $C(\phi_1, \phi_2)$ with expectation

$$\langle C(\phi_1, \phi_2) \rangle = \mathrm{Tr}[\varrho_{12}\, C(\phi_1, \phi_2)], \tag{42}$$

where ϱ_{12} is the overall density matrix associated with the four-mode state of the light beams injected into the two interferometers $\mathcal{I}_1$ and $\mathcal{I}_2$.

The two configurations used to observe the holographic noise are depicted in fig. 20. Figure 20(a) shows the parallel configuration, in which the two interferometers occupy the same space-time volume: in this case the holographic noise induces the same fluctuation on the phase shift, thus leading to a correlation of the intensity fringes. When the

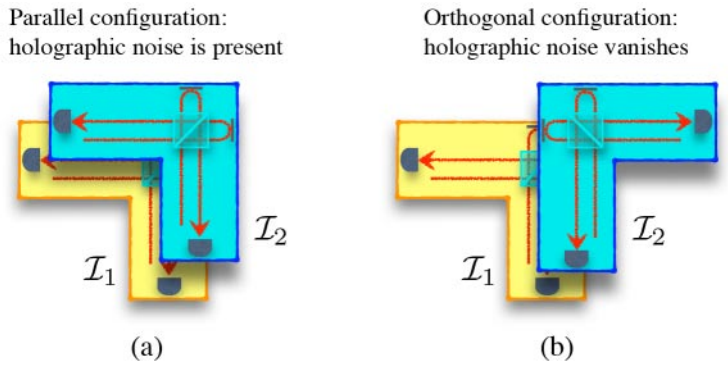

Fig. 20. – Two possible configurations of the two Michelson interferometers. (a) In the parallel configuration the interferometers are in overlapping space-time volumes: the holographic noise correlates the outputs. (b) In the orthogonal configuration the space-time volumes of the interferometers are no longer overlapping and the correlation induced by the holographic noise vanishes.

interferometers are in the orthogonal configuration, fig. 20(b), their space-time volumes are no longer overlapping and the correlation induced by the holographic noise vanishes: this can be used as a reference, that is a measurement of the "background".

Following ref. [65], we can describe the statistical properties of the phase shift fluctuations induced by the holographic noise by means of a suitable probability density function $f_x(\phi_1, \phi_2)$, $x = \parallel, \perp$. Of course, since if we address the single interferometer we cannot distinguish between the two configurations, given the marginals

$$\mathcal{F}_x^{(k)}(\phi_k) = \int f_x(\phi_1, \phi_2)\, \mathrm{d}\phi_h, \tag{43}$$

with $h, k = 1, 2$ and $h \neq k$, we should have

$$\mathcal{F}_{\parallel}^{(k)}(\phi_k) = \mathcal{F}_{\perp}^{(k)}(\phi_k); \tag{44}$$

on the other hand, since in the orthogonal configuration there are not correlations between the two interferometers, we should also require

$$f_{\perp}(\phi_1, \phi_2) = \mathcal{F}_{\parallel}^{(1)}(\phi_1)\, \mathcal{F}_{\perp}^{(2)}(\phi_2). \tag{45}$$

Therefore, the actual expectations of an operator $\mathcal{O}(\phi_1, \phi_2)$, which depends on the phase shifts, should be averaged over $f_x(\phi_1, \phi_2)$, namely

$$\langle \mathcal{O}(\phi_1, \phi_2) \rangle \to \mathcal{E}_x[\mathcal{O}(\phi_1, \phi_2)] = \int f_x(\phi_1, \phi_2)\, \langle \mathcal{O}(\phi_1, \phi_2) \rangle\, \mathrm{d}\phi_1\, \mathrm{d}\phi_2. \tag{46}$$

The information about the correlation between the two phases can be obtained by estimating the covariance in the parallel configuration, *i.e.* $\mathcal{E}_{\parallel}[\delta\phi_1, \delta\phi_2]$, where

$$\delta\phi_k = \phi_k - \phi_{k,0}, \tag{47}$$

and we introduced the central phase $\phi_{k,0}$ measured by the k-th interferometer. In the limit $\delta\phi_1, \delta\phi_2 \ll 1$ we can write [65]

$$\mathcal{E}_{\parallel}[\delta\phi_1, \delta\phi_2] \approx \frac{\mathcal{E}_{\parallel}[C(\phi_1, \phi_2)] - \mathcal{E}_{\perp}[C(\phi_1, \phi_2)]}{\langle \partial^2_{\phi_1,\phi_2} C(\phi_{1,0}, \phi_{2,0})\rangle}\,, \tag{48}$$

and we clearly see that the covariance can be estimated by measuring the difference between the expectation values of the operator $C(\phi_1, \phi_2)$ in the two configurations.

In order to observe the holographic noise, we should minimize the uncertainty associated with the measurement of the covariance, which reads (still in the limit $\delta\phi_1, \delta\phi_2 \ll 1$)

$$\mathcal{U}(\delta\phi_1, \delta\phi_2) \approx \frac{\sqrt{\mathrm{var}_{\parallel}[C(\phi_1, \phi_2)] + \mathrm{var}_{\perp}[C(\phi_1, \phi_2)]}}{|\langle \partial^2_{\phi_1,\phi_2} C(\phi_{1,0}, \phi_{2,0})\rangle|}\,, \tag{49}$$

with $\mathrm{var}_x[C(\phi_1, \phi_2)] = \mathcal{E}_x[C^2(\phi_1, \phi_2)] - \mathcal{E}_x[C(\phi_1, \phi_2)]^2$. Since

$$\mathrm{var}_{\parallel}[C(\phi_1, \phi_2)] = \mathrm{var}_{\perp}[C(\phi_1, \phi_2)] = \mathrm{var}[C(\phi_1, \phi_2)] + O(\delta\phi^2), \tag{50}$$

the zero-order contribution to the uncertainty reduces to

$$\mathcal{U}^{(0)} \approx \frac{\sqrt{2\,\mathrm{var}[C(\phi_{1,0}, \phi_{2,0})]}}{|\langle \partial^2_{\phi_1,\phi_2} C(\phi_{1,0}, \phi_{2,0})\rangle|}\,. \tag{51}$$

It is worth noting that $\mathcal{U}^{(0)}$, that is the main contribution to the uncertainty, does not depend on the fluctuations induced by the holographic noise, but only on the *intrinsic* fluctuations due to the chosen measurement and to the state sent through the interferometers. As we have also seen in sects. **3** and **4**, the choice of the measurement is strictly related to the input state and, in the following, we will show that squeezing and entanglement can provide huge advantages in terms of the achieved accuracy with respect to classical light [65].

We start considering that the two-mode input state of the k-th interferometer is excited in a coherent and a squeezed vacuum state with mean number of photons μ_k and λ_k, respectively (see appendices B and C). As discussed in sect. **4**, in this case the value of ϕ_k can be retrieved assessing the difference $D_{k,-}(\phi_k)$ of the number of photons in the two output ports of the interferometer $\mathcal{I}_k$. Therefore, we can now define

$$\Delta C(\phi_1, \phi_2) \equiv \Delta D_{1,-}(\phi_1)\, \Delta D_{2,-}(\phi_2), \tag{52}$$

where

$$\Delta D_{k,-}(\phi_k) = D_{k,-}(\phi_k) - \mathcal{E}[D_{k,-}(\phi_k)]. \tag{53}$$

If we assume $\mu_1 = \mu_2 = \mu$ and $\lambda_1 = \lambda_2 = \lambda$, and consider the optimal working regime $\phi_{1,0} = \phi_{2,0} = \pi/2$, we obtain [65]

$$\mathcal{U}^{(0)}_{\mathrm{SQ}} \approx \sqrt{2}\,\frac{\lambda + \mu(1 + 2\lambda - 2\sqrt{\lambda + \lambda^2})}{(\lambda - \mu)^2}\,, \tag{54}$$

which, in the limit $\mu \gg \lambda \gg 1$, becomes

$$\mathcal{U}_{\mathrm{SQ}}^{(0)} \approx \frac{1}{2\sqrt{2}\,\lambda\,\mu}\,. \tag{55}$$

The advantage with respect to the classical case $\mathcal{U}_{\mathrm{CL}}^{(0)} \approx \sqrt{2}/\mu$ in which only coherent states are used is thus clear. Nevertheless, in this latter case it is worth noting that the measurement on the covariance, involving *second-order momenta*, leads to a scaling $\propto \mu^{-1}$ instead of $\propto \mu^{-1/2}$ as in the case of the single interferometer.

Though the use of squeezing leads to an advantage with respect to the classical scenario, the improvement is due to the *independent* improvement of the two single interferometers. Here, however, we are interested in minimising the noise of the correlation between the interferometers. It is thus natural to investigate whether the use of quantum correlated states coupling the two interferometers can produce further improvement.

Let us now suppose to couple $\mathcal{I}_1$ and $\mathcal{I}_2$ by exciting their input modes a_1 and a_2 (see fig. 19) in the twin-beam state introduced in sect. **4** (see also appendix D) which we rewrite as

$$|\mathrm{TWB}\rangle\rangle_{a_1,a_2} = \sum_n c_n(\lambda)\,|n\rangle_{a_1}|n\rangle_{a_2}, \tag{56}$$

where λ is still the average number of photons of each mode and

$$c_n(\lambda) = \sqrt{\frac{\lambda^n}{(1+\lambda)^{n+1}}}\,. \tag{57}$$

Due to the symmetry between the two modes, we have the peculiar property

$$_{a_1,a_2}\langle\langle \mathrm{TWB}|\left(a_1^\dagger a_1 - a_2^\dagger a_2\right)^M |\mathrm{TWB}\rangle\rangle_{a_1,a_2} = 0, \quad \forall M > 0. \tag{58}$$

As in the previous case, we assume to send in the other input ports of the interferometers two equal coherent states $|\sqrt{\mu}\rangle_{b_1}|\sqrt{\mu}\rangle_{b_1}$ with average number of photons μ. Overall, we have the four-mode input state

$$|\Psi\rangle = |\mathrm{TWB}\rangle\rangle_{a_1,a_2}|\sqrt{\mu}\rangle_{b_1}|\sqrt{\mu}\rangle_{b_1}. \tag{59}$$

If we choose the working regime $\phi_{1,0} = \phi_{2,0} = 0$ and, of course, in the absence of the holographic noise, the two interferometers of the holometer behave like two *completely transparent media*, as one can easily check from the input-output relations (10): the output modes c_1 and c_2, coming from a_1 and a_2, respectively, exhibit *perfect* correlation between the number of photons.

If we now define the observable

$$C(\phi_1, \phi_2) = \Delta^2(N_{c_1} - N_{c_2}), \tag{60}$$

where $N_{c_k} = c_k^\dagger c_k$, we have $\mathrm{var}[C(\phi_{1,0}, \phi_{2,0})] = 0$ in eq. (51), whereas the denominator reads

$$|\langle\Psi|\partial^2_{\phi_1,\phi_2} C(\phi_{1,0}, \phi_{2,0})|\Psi\rangle| = \frac{1}{2}\,\mu\sqrt{\lambda + \lambda^2}. \tag{61}$$

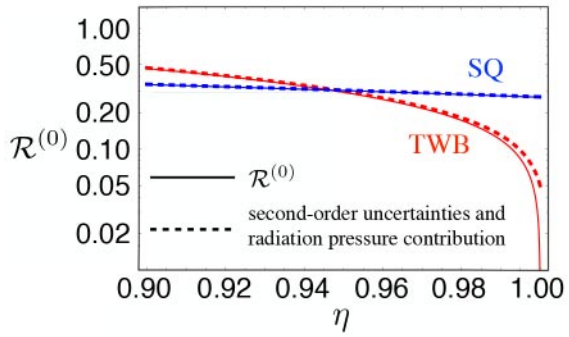

Fig. 21. – Plot of the ratio $\mathcal{R}^{(0)} = \mathcal{U}^{(0)}/\mathcal{U}^{(0)}_{\rm CL}$ as a function of the overall transmission-detection efficiency η for the squeezed vacua and the twin beams (solid lines). We consider the realistic values $\mu = 2\times 10^{23}$ for the coherent state intensities and $\lambda = 0.5$ for the squeezed vacua and each of the twin beams. The dashed lines refer to the second-order uncertainties where we also added the radiation pressure contribution. Here we considered a mirror mass 10^2 kg and a central light frequency $\omega = 3.14 \times 10^{15}$ Hz (corresponding to a wavelength of 600 nm) and a measurement time of 10^{-3} s. Adapted from ref. [65].

Therefore, if $\mu, \lambda \neq 0$ we find the following striking result:

$$\mathcal{U}^{(0)}_{\rm TWB} = 0. \tag{62}$$

Remarkably, the perfect correlation existing between the two beams leads to a vanishing zero-order contribution to the uncertainty of the covariance. In this scenario any very faint perturbation which correlates the interferometers can be detected, since it cannot be masked by a residual noise. We note that in the presence of fluctuations due to the holographic noise, a little portion of the coherent states is reflected to the monitored ports, thus guaranteeing the sensitivity to the covariance of the holographic noise phase shift.

As a matter of fact, in real experiments we should also consider other effects which may affect the ideal results obtained above. One of the main contributions which can increase the uncertainty of the covariance measurement is a non-unit overall transmission-detection efficiency η (see appendix E). In fig. 21 the ratio

$$\mathcal{R}^{(0)} = \frac{\mathcal{U}^{(0)}}{\mathcal{U}^{(0)}_{\rm CL}} \tag{63}$$

is shown as a function of η for the squeezed vacua and the twin beams (solid lines). We can see that there exists a threshold on η (that depends on the other involved parameters) above which the measurement involving the twin beams outperforms both the classical strategy and the one based on uncorrelated squeezed vacua. In this region of high efficiency we have a significant reduction of the uncertainty. Moreover, our analysis proves that also below that threshold nonclassical squeezed light beats the performance of classical coherent light. In the limit $\mu \gg 1$ and $\lambda \ll 1$ (as considered in fig. 21), we find

$$\mathcal{R}^{(0)}_{\rm SQ} = \frac{\mathcal{U}^{(0)}_{\rm SQ}}{\mathcal{U}^{(0)}_{\rm CL}} \approx 1 - 2\eta\sqrt{\lambda} \quad (\mu \gg 1, \lambda \ll 1), \tag{64}$$

whereas

$$\mathcal{R}^{(0)}_{\mathrm{TWB}} = \frac{\mathcal{U}^{(0)}_{\mathrm{TWB}}}{\mathcal{U}^{(0)}_{\mathrm{CL}}} \approx \sqrt{\frac{2(1-\eta)}{\eta}} \quad (\mu \gg 1, \lambda \ll 1), \tag{65}$$

and an improvement with respect the classical case can be obtained for $\eta > 2/3 \approx 0.67$. On the other hand, if $\mu \gg \lambda \gg 1$ we obtain

$$\mathcal{R}^{(0)}_{\mathrm{SQ}} \approx (1-\eta) - \frac{\eta}{4\lambda} \quad (\mu \gg \lambda \gg 1), \tag{66}$$

and

$$\mathcal{R}^{(0)}_{\mathrm{TWB}} \approx 2\sqrt{5}(1-\eta) \quad (\mu \gg \lambda \gg 1). \tag{67}$$

Therefore, also in this case the approach based on twin beams outperforms the classical one (for $\eta > 0.776$) and the uncertainty drop to zero as $\eta \to 1$.

For the sake of completeness, in fig. 21 we also plot the uncertainty reduction normalised to $\mathcal{U}^{(0)}_{\mathrm{CL}}$ as a function of η (dashed lines) considering the second-order uncertainties and the radiation pressure contribution [73]. We recall that in the case of a single interferometer fed by squeezed light, the amplitude of the noise due to the radiation pressure decreases as the squeezing parameter increases. In the present case we have an analogue behaviour. If we consider reasonable values of the involved parameters, the radiation pressure noise is completely negligible. We can see in fig. 21 that for the realistic parameters we have chosen we have just a very small correction. The reader can find further details about this last point in ref. [65].

Remarkably, our results not only demonstrate that the use of quantum and entangled states of light allows reaching much higher sensibility for the realisation of experiments to test quantum gravity, but also put forward new opportunities for the design of innovative interferometric schemes, as we will discuss in the next section.

8. – Squeezed and entangled light in correlated interferometry

The experimental requirements to implement the double-interferometer setup introduced in the previous section are extremely challenging. In particular, one should control the working regimes of the interferometers with a very high accuracy in order to obtain the huge advantages given by twin beams. Moreover, the quantum efficiency η must be greater than ≈ 0.99 (see fig. 21).

We have seen that to exploit the twin-beam properties to reduce the uncertainty in the covariance measurement, we should choose a regime in which the interferometers act like transparent media. We recall that if ϕ_k is the measured phase, the interferometer $\mathcal{I}_k$ is equivalent to a beam splitter with transmissivity $\tau_k = \cos^2(\phi_k/2)$ (the interferometer transmission). The coherent amplitude which usually circulates in the interferometers is so high that also a small reflection probability $1 - \tau_k$ can send a really high number of photons to the measured ports. For instance, if only coherent states with energy μ are considered and, therefore, the input state is

$$|0\rangle_{a_1}|0\rangle_{a_2}|\sqrt{\mu}\rangle_{b_1}|\sqrt{\mu}\rangle_{b_2}, \tag{68}$$

we have

$$\langle N_k\rangle^{\rm coh}_{\eta\tau_k} = \langle \delta N_k^2\rangle^{\rm coh}_{\eta\tau_k} = \eta\mu(1-\tau_k), \tag{69a}$$

$$\langle \delta N_1 \delta N_2\rangle^{\rm coh}_{\eta\tau_1\tau_2} \equiv 0, \tag{69b}$$

where $N_k = c_k^\dagger c_k$, $k = 1, 2$, $\delta\mathcal{O} = \mathcal{O} - \langle\mathcal{O}\rangle$, $\delta\mathcal{O}^2 = \mathcal{O}^2 - \langle\mathcal{O}\rangle^2$ and η is the quantum efficiency of the detectors (see appendix E). We assume, for the sake of simplicity, that they have the same quantum efficiency. On the other hand, when we send only the twin beams to correlate the interferometer the four-mode input state is

$$|{\rm TWB}\rangle\rangle_{a_1,a_2}|0\rangle_{b_1}|0\rangle_{b_2}, \tag{70}$$

and we find

$$\langle N_k\rangle^{\rm TWB}_{\eta\tau_k} = \eta\tau_k\lambda, \tag{71a}$$

$$\langle \delta N_k^2\rangle^{\rm TWB}_{\eta\tau_k} = \eta\tau_k\lambda(1+\eta\tau_k\lambda), \tag{71b}$$

$$\langle \delta N_1 \delta N_2\rangle^{\rm TWB}_{\eta\tau_1\tau_2} = \eta^2\tau_1\tau_2\lambda(1+\lambda), \tag{71c}$$

where we used the same parametrization as in sect. **6**.

Following ref. [66], we introduce the noise reduction parameter

$${\rm NRF}_\pm = \frac{\langle\delta(N_1 \pm N_2)^2\rangle}{\langle N_1 + N_2\rangle}, \tag{72}$$

that is the ratio between the variance of the sum or difference between the detected photon numbers and the corresponding shot-noise limit. Since a value ${\rm NRF}_- < 1$ is a signature of nonclassical correlations while ${\rm NRF}_+ < 1$ denotes anticorrelations of the photon number beyond the classical limits, we can use ${\rm NRF}_\pm$ as a figure of merit for the correlations at the output ports.

When we consider as input state $|{\rm TWB}\rangle\rangle_{a_1,a_2}|\sqrt{\mu}\,e^{i\psi}\rangle_{b_1}|\sqrt{\mu}\,e^{i\psi}\rangle_{b_2}$, by using eqs. (10), (69) and (71) we can easily find

$$\langle N_k\rangle = \langle N\rangle^{\rm TWB}_{\eta\tau_k} + \langle N\rangle^{\rm coh}_{\eta\tau_k}, \tag{73a}$$

$$\langle \delta N_k^2\rangle = \langle \delta N^2\rangle^{\rm TWB}_{\eta\tau_k} + \langle \delta N^2\rangle^{\rm coh}_{\eta\tau_k} + 2\langle N\rangle^{\rm TWB}_{\eta\tau_k}\langle N\rangle^{\rm coh}_{\eta\tau_k}, \tag{73b}$$

$$\langle \delta N_1 \delta N_2\rangle = \langle \delta N_1 \delta N_2\rangle^{\rm TWB}_{\eta\tau_1\tau_2} - 2\sqrt{\langle \delta N_1 \delta N_2\rangle^{\rm TWB}_{\eta\tau_1\tau_2}\langle N\rangle^{\rm coh}_{\eta\tau_1}\langle N\rangle^{\rm coh}_{\eta\tau_2}}\cos(2\psi). \tag{73c}$$

It is interesting to note that the covariance $\langle\delta N_1\delta N_2\rangle$ depends on the coherent fields phase ψ: if we set $\psi = \pi/2$ the covariance is maximised whereas if $\psi = 0$, we can also have a negative value for $\langle\delta N_1\delta N_2\rangle$, corresponding to an anticorrelation of photon numbers. We can now write explicitly the expression of the noise reduction factor, namely (we set for the sake of simplicity $\tau_1 = \tau_2 = \tau$):

$${\rm NRF}_\pm = \frac{\frac{1}{2}\langle\delta(N_1 \pm N_2)^2\rangle^{\rm TWB}_{\eta\tau} + 2\langle N\rangle^{\rm coh}_{\eta\tau}\left[\frac{1}{2} + \langle N\rangle^{\rm TWB}_{\eta\tau} \mp \sqrt{\langle\delta N_1\delta N_2\rangle^{\rm TWB}_{\eta\tau}}\cos(2\psi)\right]}{\langle N\rangle^{\rm TWB}_{\eta\tau} + \langle N\rangle^{\rm coh}_{\eta\tau}}. \tag{74}$$

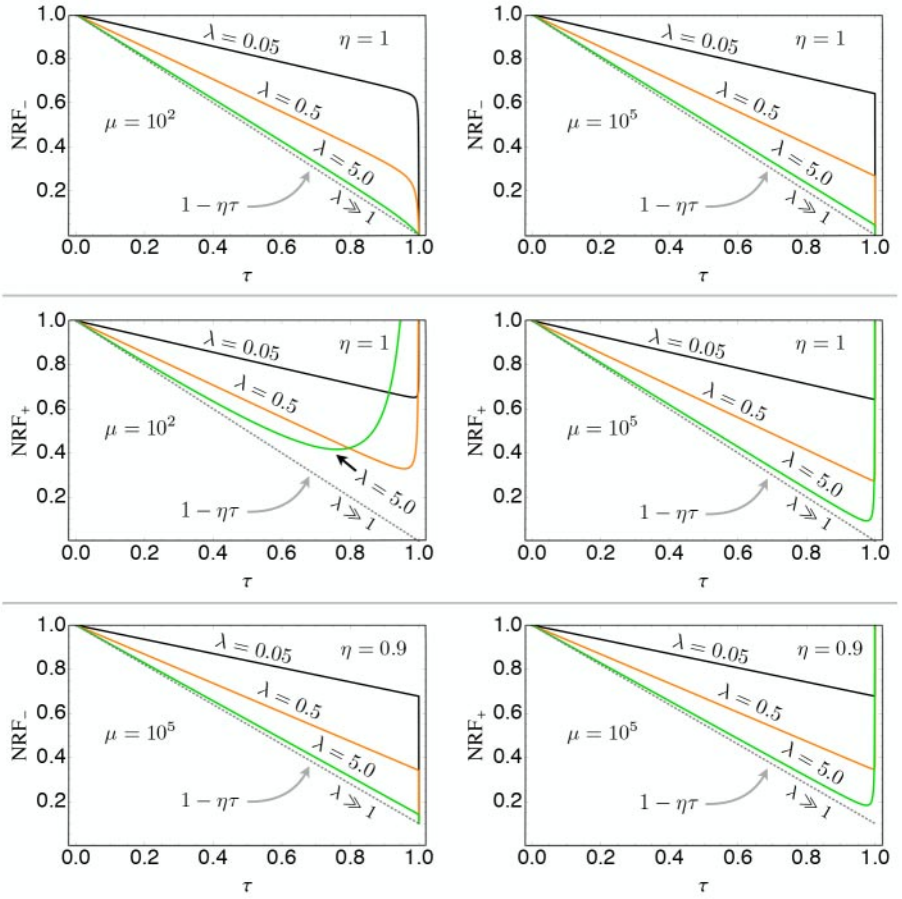

Fig. 22. – Top: plot of the maximised (*i.e.* $\psi = \pi/2$) NRF_- as a function of the overall interferometer transmission τ for different values of the twin-beam energy per beam λ and for $\mu = 10^2$ (left panel) and $\mu = 10^5$ (right panel). We set $\eta = 1$. Centre: plot of the maximised (*i.e.* $\psi = 0$) NRF_+ as a function of the overall interferometer transmission τ for different values of the twin-beam energy per beam λ and for $\mu = 10^2$ (left panel) and $\mu = 10^5$ (right panel). We set $\eta = 1$. Bottom: plot of $\mathrm{NRF}_\pm$ with the same parameters as in the other plots but with $\eta = 0.9$. In all the panels the dotted line refers to $\mathrm{NRF}_\pm$ in the limit $\lambda \gg 1$.

It is clear that the condition $\psi = \pi/2$ (optimising of the photon number correlation) minimises NRF_-, while $\psi = 0$ (optimising of the anticorrelation) minimises NRF_+: from now on we consider these optimising conditions when we refer to the $\mathrm{NRF}_\pm$. In fig. 22 we plot the $\mathrm{NRF}_\pm$ as a function of $\tau_1 = \tau_2 = \tau$ and different values of the other parameters.

Since we are considering correlations, it is natural to identify two regimes. The first one corresponds to the regime studied in sect. **6**, in which $\kappa \equiv \mu(1-\tau)/\tau\lambda \ll 1$, corresponding to $\langle N \rangle_{\eta\tau}^{\mathrm{coh}} \ll \langle N \rangle_{\eta\tau}^{\mathrm{TWB}}$. In this case the intensity arriving at the detectors is dominated by the twin beams and, as one may expect from the results of sect. **6**, NRF_- drastically decreases whereas NRF_+ grows (see fig. 22 for $\tau \to 1$). If we expand

the noise reduction factor up to the first order in $1-\tau$ we have

$$\mathrm{NRF}_- \approx 1-\eta+\eta(1-\tau)\left[1+2\mu+\frac{\mu(1-2\sqrt{\lambda^2+\lambda})}{\lambda}\right], \tag{75}$$

and

$$\mathrm{NRF}_+ \approx 1+\eta(1+2\lambda)+\eta(\tau-1)\left[1+2\lambda+\frac{\mu(1-2\sqrt{\lambda^2+\lambda})}{\lambda}\right], \tag{76}$$

respectively, and we used, as mentioned above, the corresponding optimising values of ψ. In the limit $\lambda \gg 1$ we also have

$$\mathrm{NRF}_- \approx 1-\eta\tau, \tag{77a}$$

$$\mathrm{NRF}_+ \approx 1+\eta\tau(1+2\lambda). \tag{77b}$$

Overall, this regime allows obtaining a huge quantum enhancement in phase correlation measurement by exploiting the twin-beam correlations also in the presence of a large classical power circulating into the interferometer.

In the other regime we have $\mu(1-\tau) \gg \lambda\tau$ and, thus, $\langle N\rangle_{\eta\tau}^{\mathrm{coh}} \gg \langle N\rangle_{\eta\tau}^{\mathrm{TWB}}$. Now (still considering the corresponding optimizing values of ψ) we find

$$\mathrm{NRF}_\pm \approx 1-2\eta\tau\left[\sqrt{\lambda(1+\lambda)}-\lambda\right] < 1, \tag{78}$$

which, in the limit $\lambda \gg 1$ reduces to $\mathrm{NRF}_\pm \approx 1-\eta\tau$ (see the dotted lines in fig. 22). Since $\mathrm{NRF}_\pm < 1$, the number of photons are always correlated or anticorrelated beyond the classical limit. It is worth noting that this correlation can be also really bright, since, in real experiments, $\langle N\rangle_{\eta\tau}^{\mathrm{coh}} = \eta\mu(1-\tau)$ can be very large [66].

We now focus our attention of the effect of small deviations from the optimal working regime $\phi_0 = \phi_{1,0} = \phi_{2,0} = 0$ on the ratio $\mathcal{R}^{(0)}$ between the quantum and the classical uncertainties of the covariance estimation introduced in the previous section (see fig. 21). Since we are interested in having strong nonclassical correlations, we set $\psi = \pi/2$ and consider the limit $\mu \gg 1$. In fact, a quantum strategy is supposed to enhance the sensitivity when high power is circulating in the interferometer. The results are plotted in figs. 23 and 24 for both the twin beams and two independent squeezed vacua as inputs (and, of course, the coherent states).

In the case of twin beams (left panels of figs. 23 and 24) we can in general identify two regions: one for $\phi_0 < 10^{-6}$ and the other for $10^{-5} < \phi_0 < 10^{-1}$. These regions depend on the choice of the involved parameters and their relations.

If ϕ_0 is very small, the interferometer transmissivities are high and, thus, we have the regime $\langle N\rangle_{\eta\tau}^{\mathrm{coh}} \ll \langle N\rangle_{\eta\tau}^{\mathrm{TWB}}$ in which twin-beam correlations are predominant. This is the regime considered in the previous section and in ref. [65]. In the second region, for $10^{-5} < \phi_0 < 10^{-1}$, the transmissivity of the interferometers is such that the regime of bright quantum correlation $\langle N\rangle_{\eta\tau}^{\mathrm{coh}} \ll \langle N\rangle_{\eta\tau}^{\mathrm{TWB}}$ is reached: we find a flat $\mathcal{R}_{\mathrm{TWB}}^{(0)}$.

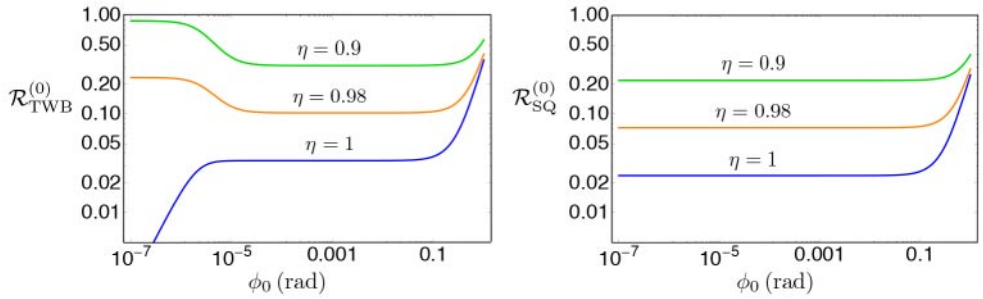

Fig. 23. – Log-log plot of the ratios $\mathcal{R}^{(0)}_{\rm TWB}$ (left) and $\mathcal{R}^{(0)}_{\rm SQ}$ (right) as functions of the central phase ϕ_0 measured by the interferometers and different values of the detection efficiency η. When $\mathcal{R}^{(0)} < 1$ we have an advantage with respect to the classical case. We set $\lambda = 10$, $\mu = 3 \times 10^{12}$ and $\psi = \pi/2$.

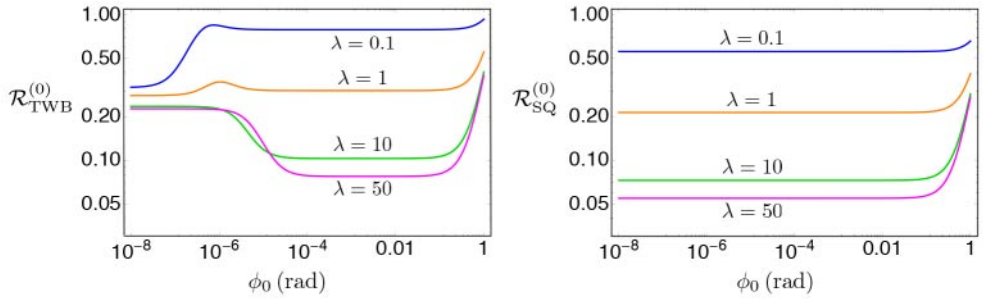

Fig. 24. – Log-log plot of the ratios $\mathcal{R}^{(0)}_{\rm TWB}$ (left) and $\mathcal{R}^{(0)}_{\rm SQ}$ (right) as functions of the central phase ϕ_0 measured by the interferometers and different values of the detection efficiency λ. When $\mathcal{R}^{(0)} < 1$ we have an advantage with respect to the classical case. We set $\eta = 0.95$, $\mu = 3 \times 10^{12}$ and $\psi = \pi/2$.

When we consider two independent squeezed states instead of the twin beams (see the right panels of figs. 23 and 24) we can write the following expansions for $\mu \gg 1$ [66]:

$$\mathcal{R}^{(0)}_{\rm SQ} \approx 1 - \frac{\eta(1+\cos\phi_0)}{2} + \frac{\eta\cos^2(\phi_0/2)}{4\lambda} \quad \text{if } \lambda \gg 1, \tag{79a}$$

$$\mathcal{R}^{(0)}_{\rm SQ} \approx 1 - \eta(1+\cos\phi_0)\sqrt{\lambda}(1-\sqrt{\lambda}) \quad \text{if } \lambda \ll 1, \tag{79b}$$

that are both less than 1 and, thus, show the advantage of using quantum light. From these expansions and from the right panel of figs. 23 and 24, we can see that the best results are obtained for ϕ_0 very close to 0. Moreover, if we consider the interval of phase values $10^{-5} < \phi_0 < 10^{-1}$ in the limit $\mu \gg 1$, we have $\mathcal{R}^{(0)}_{\rm TWB} \approx \sqrt{2}\,\mathcal{R}^{(0)}_{\rm SQ}$.

In the left panel of fig. 25 we plot the ratio $\mathcal{R}^{(0)}$ for the twin beams (solid lines) and the squeezed states (dashed lines) as functions of η and a particular choice of the other involved parameters. There exists a threshold value $\eta_{\rm th}$ of the quantum efficiency such that for $\eta > \eta_{\rm th}$ the strategy based on twin beams outperforms the one exploiting independent squeezed states (see fig. 25, right panel).

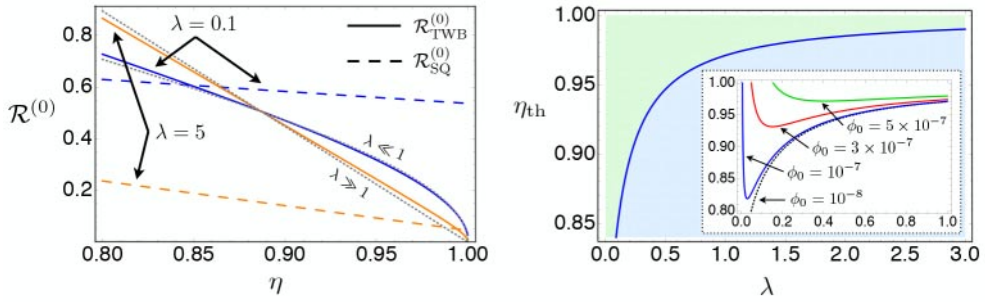

Fig. 25. – Left: plot of the ratio $\mathcal{R}^{(0)}_{\rm TWB}$ (solid lines) and $\mathcal{R}^{(0)}_{\rm SQ}$ (dashed lines) as a function of the detection efficiency η for two different values of the average number of photons per single mode λ of the twin beams and the squeezed sates. The grey dotted lines refer to $\mathcal{R}^{(0)}_{\rm TWB}$ in the limits $\lambda \gg 1$ and $\lambda \ll 1$. Right: plot of the threshold value $\eta_{\rm th}$ as a function of λ: if $\eta > \eta_{\rm th}$ then $\mathcal{R}^{(0)}_{\rm TWB} < \mathcal{R}^{(0)}_{\rm SQ}$ (upper shaded region of the plot). The inset shows $\eta_{\rm th}$ as a function of λ (we dropped the axes labels) for different values of ϕ_0 (the dotted line is the same as the main plot). In both the panels we set $\mu = 3 \times 10^{12}$, $\psi = \pi/2$ and $\phi_0 = 10^{-8}$.

Overall, we can conclude that quantum light injected into the free ports of interferometers is a useful and practical resource to improve the measurement of phase-correlation covariance. On the one hand, the results obtained for two interferometers confirm the advantage of exploiting squeezed beams and highly excited coherent states at the inputs. This is the analogue of the case of single interferometers considered in sect. **4**. On the other hand, the promising results concerning the twin beams show that there is room for realistic applications of bipartite continuous-variable entanglement in interesting and unexplored areas requiring high-precision correlation measurements, such as the test of quantum gravity theories.

9. – Conclusion

In these pages we have presented some of the theoretical and experimental results obtained by applying the tools of classical and quantum estimation theory to optical systems. Firstly, we have investigated the role of single- and two-mode squeezing in active and passive interferometers, finding the regimes in which quantum resources can improve the sensitivity of the interferometer also in the presence of losses. Then we have considered a quantum illumination protocol where two quantum correlated beams are used to detect the presence of an object embedded in a very noisy and predominant background. Also in this case the theoretical and experimental results show that the use of quantum light outperforms schemes based on classical correlated beams. Eventually, our research was focused on interferometric schemes involving two interferometers. This kind of setup has been recently proposed to test the effects of the noncommutativity of the position and momentum operators at the Planck scale predicted by a quantum gravity theory, giving birth to the so-called holographic noise. We have theoretically shown that coupling the two interferometers by means of two continuous-variable entangled beams can improve the sensitivity to the holographic noise or, more in general, to the correlation measurements.

The quest for advanced schemes to measure a phase shift with high accuracy, to detect the presence of an evanescent object in a noisy environment or to unveil very

faint and subtle phenomena that may confound with the background is indeed amazing and always brings to new exiting results (also thanks to technological advances). The research we reviewed in this paper shows that there is room for innovative, quantum-enhanced schemes which can shed new light not only on well-known areas, but also on still unexplored realms.

* * *

As any researcher knows, "this is not just our work, but our dream and a big part of our life". The author would like to express his gratitude to all the scientists involved in the "Light Correlations for High-precision Innovative Sensing – LiCHIS" project (funded by MIUR through the FIRB project nr. RBFR10YQ3) which has led to most of the results presented in these pages and, in particular, to Alessia Allevi, Alice Meda, Matteo Bina, Ivano Ruo-Berchera, Ivo P. Degiovanni, Carlo Sparaciari, Maria Bondani, Marco Genovese and Matteo G. A. Paris. Useful and stimulating discussions with the people of the Quantum Technology Lab of the University of Milan are also kindly acknowledged and, among them, with Claudia Benedetti, Fabrizio Castelli, Simone Cialdi, Marco G. Genoni, Nicola Piovella and Dario Tamascelli.

Appendix A.

Beam splitter

The beam splitter is a common device we can find in any quantum optics experiment. The Hamiltonian describing the beam splitter interaction can be written as $\mathcal{H} = g a^\dagger b + g^* a b^\dagger$, g being the coupling constant, and involves the two input bosonic field operators, a and b, with commutation relations $[a, a^\dagger] = \mathbb{I}$ and $[b, b^\dagger] = \mathbb{I}$, respectively, and $[a, b] = 0$. For the sake of simplicity, we write the corresponding evolution operator as

$$U_{\rm BS}(\zeta) = \exp\left(\zeta\, a^\dagger b - \zeta^*\, a b^\dagger\right), \tag{A.1}$$

where $\zeta = \phi\, e^{i\theta}$. To write the evolution operator in the form (A.1) we applied the transformation $a \to -ia$ which physically corresponds to impose a $\pi/2$ phase shift to the mode a, namely $U^\dagger_{\rm ph}(\pi/2)\, a\, U_{\rm ph}(\pi/2) = -ia$, where $U_{\rm ph}(\varphi) = \exp(-i\varphi\, a^\dagger a)$ is the phase-shift operator and, in general

$$U^\dagger_{\rm ph}(\varphi)\, a\, U_{\rm ph}(\varphi) = a\, e^{-i\varphi}. \tag{A.2}$$

In order to calculate the Schrödinger evolution of two states through a beam splitter by applying $U_{\rm BS}(\zeta)$, we note that the two-boson operators

$$J_+ = a^\dagger b, \qquad J_- = a b^\dagger \qquad \text{and} \qquad J_3 = \frac{1}{2}[J_+, J_-] = \frac{1}{2}(a^\dagger a - b^\dagger b) \tag{A.3}$$

are a realisation of the SU(2) algebra. Therefore, we can rewrite eq. (A.1) as follows:

$$U_{\rm BS}(\zeta) = \exp\left[e^{i\theta}\tan\phi\, a^\dagger b\right]\, \left(\cos^2\phi\right)^{(a^\dagger a - b^\dagger b)/2} \exp\left[-e^{-i\theta}\tan\phi\, a b^\dagger\right], \tag{A.4a}$$

$$= \exp\left[-e^{-i\theta}\tan\phi\, a b^\dagger\right]\, \left(\cos^2\phi\right)^{-(a^\dagger a - b^\dagger b)/2} \exp\left[e^{i\theta}\tan\phi\, a^\dagger b\right], \tag{A.4b}$$

Sometimes it is also useful to study the Heisenberg evolution of the input modes. In this case we can use the identity:

$$e^{A}\, B\, e^{-A} = B + [A,B] + \frac{1}{2!}\,[A,[A,B]] + \frac{1}{3!}\,[A,[A,[A,B]]] + \cdots\,, \tag{A.5}$$

which holds for two operators A and B. In the presence of the beam splitter, we obtain

$$U_{\mathrm{BS}}^{\dagger}(\zeta)\, a\, U_{\mathrm{BS}}(\zeta) = a\cos\phi + b\, e^{i\theta}\sin\phi, \tag{A.6a}$$

$$U_{\mathrm{BS}}^{\dagger}(\zeta)\, b\, U_{\mathrm{BS}}(\zeta) = b\cos\phi - a\, e^{-i\theta}\sin\phi, \tag{A.6b}$$

It is therefore clear that, due to the action of the beam splitter, each mode evolves into a linear combination of the input modes and, for this reason, this kind of interaction is also called *two-mode mixing interaction*. The quantity $\tau = \cos^2\phi$ is usually called transmissivity of the beam splitter.

A *mirror* can be seen as a beam splitter with reflectivity equal to 1. Therefore, by setting $\phi = \pi/2$ and $\theta = 0$, we find the following mode transformations:

$$U_{\mathrm{BS}}^{\dagger}(\pi/2)\, a\, U_{\mathrm{BS}}(\pi/2) = b, \tag{A.7a}$$

$$U_{\mathrm{BS}}^{\dagger}(\pi/2)\, b\, U_{\mathrm{BS}}(\pi/2) = -a. \tag{A.7b}$$

We note that the results described in this appendix depend on the phase-shift transformation we initially applied to the mode a to write the beam splitter evolution operator in the form (A.1).

Appendix B.

Coherent states

The coherent states are the closest approximation of the output state of a laser and are the eigenvectors of the annihilation operator a, namely

$$a|\alpha\rangle = \alpha|\alpha\rangle, \quad \alpha \in \mathbb{C}. \tag{B.1}$$

Exploiting the completeness relation $\sum_n |n\rangle\langle n| = \mathbb{I}$ and the normalisation condition $\langle\alpha|\alpha\rangle = 1$, we can find the photon number expansion of a coherent state, which reads

$$|\alpha\rangle = e^{-|\alpha|^2/2} \sum_{n=0}^{\infty} \frac{\alpha^n}{\sqrt{n!}} |n\rangle, \tag{B.2}$$

and the photon number distribution is

$$p(n) = |\langle n|\alpha\rangle|^2 = e^{-|\alpha|^2}\, \frac{|\alpha|^{2n}}{n!}\,, \tag{B.3}$$

that is a Poisson distribution with average number of photons $N = \langle a^{\dagger}a\rangle = |\alpha|^2$ and variance $\mathrm{var}[N] = \langle (a^{\dagger}a)^2\rangle - \langle a^{\dagger}a\rangle^2 = |\alpha|^2$.

Coherent states can be obtained by applying the so-called displacement operator $\mathcal{D}(\alpha)$ to the vacuum state $|0\rangle$. The displacement operator is defined as

$$\mathcal{D}(\alpha) = \exp\left(\alpha a^\dagger - \alpha^* a\right). \tag{B.4}$$

Given two operators A and B such that $[A, B] \in \mathbb{C}$, we have

$$\exp(A+B) = \exp(A)\exp(B)\exp\left\{-\frac{1}{2}[A,B]\right\}, \tag{B.5a}$$

$$= \exp(B)\exp(A)\exp\left\{\frac{1}{2}[A,B]\right\}. \tag{B.5b}$$

If we use eqs. (B.5) to evaluate $\mathcal{D}(\alpha)|0\rangle$ we have

$$\mathcal{D}(\alpha)|0\rangle = e^{-|\alpha|^2/2}\exp(\alpha a^\dagger)\underbrace{\exp(\alpha^* a)|0\rangle}_{|0\rangle}, \tag{B.6a}$$

$$= e^{-|\alpha|^2/2}\sum_{n=0}^{\infty}\frac{1}{n!}\left(\alpha a^\dagger\right)^n|0\rangle, \tag{B.6b}$$

$$= e^{-|\alpha|^2/2}\sum_{n=0}^{\infty}\frac{\alpha^n}{\sqrt{n!}}|n\rangle, \tag{B.6c}$$

that is $\mathcal{D}(\alpha)|0\rangle = |\alpha\rangle$.

Other useful properties of the coherent states concern the expectation values of the quadrature operator

$$X_\theta = a\, e^{-i\theta} + a^\dagger\, e^{i\theta}. \tag{B.7}$$

Given the coherent state $|\alpha\rangle$, we have

$$\langle X_\theta\rangle = \langle\alpha|X_\theta|\alpha\rangle = 2\,\Re\mathrm{e}[\alpha\, e^{-i\theta}], \tag{B.8}$$

for the first moment and

$$\mathrm{var}[X_\theta] = \langle X_\theta^2\rangle - \langle X_\theta\rangle^2 = 1, \tag{B.9}$$

for the variance which is independent of both the quadrature phase θ and the coherent state amplitude α. It is interesting to note that $\mathrm{var}[X_\theta] = 1$ also for $|\alpha\rangle = |0\rangle$, that is in the presence of the vacuum state: the value $\mathrm{var}[X_\theta] = 1$ is sometimes called the "vacuum noise" or the "shot noise"([1]).

Coherent states are *minimum uncertainty* states. In fact, in general we have

$$\mathrm{var}[X]\,\mathrm{var}[P] \geq 1, \tag{B.10}$$

([1]) It is worth noting that the actual value of $\mathrm{var}[X_\theta]$ depends on the definition of the quadrature X_θ. In general, if we define $X_\theta = \sigma_0(a\, e^{-i\theta} + a^\dagger\, e^{i\theta})$ we obtain, for a coherent state, $\mathrm{var}[X_\theta] = \sigma_0^2$.

where $X = X_0$ and $P = X_{\pi/2}$. As a matter of fact, the inequality (B.10) reaches the minimum for coherent states, since $\mathrm{var}[X] = \mathrm{var}[P] = 1$. Nevertheless, there exists another class of minimum uncertainty states, the squeezed states, which will be introduced in the following.

Appendix C.

Single-mode squeezed states

A state is called "squeezed" if the value of a quadrature variance is less than the vacuum state one (in the present case less than 1). The Hamiltonian associated with single-mode squeezing has the form $\mathcal{H} = g(a^\dagger)^2 + g^* a^2$ and the corresponding evolution operator can be written as

$$S(\xi) = \exp\left[\frac{1}{2}\xi(a^\dagger)^2 - \frac{1}{2}\xi^* a^2\right], \tag{C.1}$$

where $\xi = r\, e^{i\psi}$. Upon introducing the operators

$$\hat{K}_+ = \frac{1}{2}(a^\dagger)^2, \qquad \hat{K}_- = \frac{1}{2}a^2, \qquad \text{and} \qquad \hat{K}_3 = -\frac{1}{2}[\hat{K}_+, \hat{K}_-] = \frac{1}{2}\left(a^\dagger a + \frac{1}{2}\right), \tag{C.2}$$

we obtain a boson realisation of SU(1, 1) algebra. Therefore we have the following identity:

$$S(\xi) = \exp\left[\frac{\nu}{2\mu}(a^\dagger)^2\right]\, \mu^{-(a^\dagger a + \frac{1}{2})} \exp\left[-\frac{\nu^*}{2\mu}a^2\right], \tag{C.3}$$

where $\mu = \cosh r$ and $\nu = e^{i\psi}\sinh r$. It is straightforward to show that

$$S^\dagger(\xi)\, a\, S(\xi) = \mu a + \nu a^\dagger, \tag{C.4}$$

and if we apply the squeezing operator to the vacuum state, we obtain the so-called *squeezed vacuum*, namely

$$S(\xi)|0\rangle = |0, \xi\rangle, \tag{C.5a}$$

$$= \frac{1}{\sqrt{\mu}} \sum_{n=0}^{\infty} \left(\frac{\nu}{2\mu}\right)^n \frac{\sqrt{(2n)!}}{n!}\, |2n\rangle. \tag{C.5b}$$

It is easy to show that the squeezed vacuum has the following relevant properties:

$$\langle N\rangle = \sinh^2 r; \tag{C.6a}$$

$$\mathrm{var}[N] = 2\sinh^2 r(\sinh^2 r + 1); \tag{C.6b}$$

$$\langle X_\theta\rangle = 0, \quad \forall\theta; \tag{C.6c}$$

$$\mathrm{var}[X_\theta] = e^{2r}\cos^2(\theta - \psi/2) + e^{-2r}\sin^2(\theta - \psi/2), \tag{C.6d}$$

where we set $\xi = r\,e^{i\psi}$. If we assume, without loss of generality, a real squeezing parameter, *i.e.* $\xi = r \in \mathbb{R}$, we have

$$\text{var}[X] = e^{2r}, \qquad \text{var}[P] = e^{-2r} \Rightarrow \text{var}[X]\,\text{var}[P] = 1, \tag{C.7}$$

that is the state $|0, r\rangle$ is a minimum uncertainty state where one of the quadratures, X, has fluctuations larger than the vacuum one (for positive r) while for the other, P, the fluctuations are lower. The reader can prove that also the *displaced squeezed state*

$$|\alpha, \xi\rangle = \mathcal{D}(\alpha) S(\xi)|0\rangle \tag{C.8}$$

is still a minimum uncertainty state with quadrature variance given by eq. (C.6*d*) but with $\langle X_\theta\rangle = 2\,\Re\text{e}[\alpha\, e^{-i\theta}] \neq 0$ (note that $\langle X_\theta\rangle$ does not depend on the squeezing parameter ξ but only on the displacement amplitude α).

Appendix D.

Two-mode squeezed states

The Hamiltonian leading to two-mode squeezing is $\mathcal{H} = g a^\dagger b^\dagger + g^* a b$, which is similar to the single-mode squeezing one introduced in appendix C, but now it involves two different modes of the radiation field. The evolution operator can be written as

$$S_2(\xi) = \exp\left(\xi a^\dagger b^\dagger - \xi^* a b\right), \tag{D.1}$$

where $\xi = r\,e^{i\psi}$. We can obtain a realisation of SU(1, 1) algebra by introducing the operators

$$\hat{K}_+ = a^\dagger b^\dagger, \qquad \hat{K}_- = ab, \qquad \text{and} \qquad \hat{K}_3 = -\frac{1}{2}[\hat{K}_+, \hat{K}_-] = \frac{1}{2}(a^\dagger a + b^\dagger b + 1). \tag{D.2}$$

Therefore, as in the case of single-mode squeezing, we have

$$S_2(\xi) = \exp\left(\frac{\nu}{\mu} a^\dagger b^\dagger\right) \mu^{-(a^\dagger a + b^\dagger b + 1)/2} \exp\left(-\frac{\nu^*}{\mu} a b\right), \tag{D.3}$$

where $\mu = \cosh r$ and $\nu = e^{i\psi} \sinh r$. Under the action of $S_2(\xi)$ the field operators a and b transform as follows:

$$S_2^\dagger(\xi)\, a\, S_2(\xi) = \mu a + \nu b^\dagger \qquad \text{and} \qquad S_2^\dagger(\xi)\, b\, S_2(\xi) = \mu b + \nu^* a^\dagger. \tag{D.4}$$

In analogy to the squeezed vacuum state, if we apply the two-mode squeezing operator to the vacuum state we obtain the *two-mode squeezed vacuum*, namely

$$S_2(\xi)|0\rangle = \frac{1}{\sqrt{\mu}} \sum_{n=0}^{\infty} \left(\frac{\nu}{\mu}\right)^n |n\rangle|n\rangle, \tag{D.5}$$

or, if we introduce the parameter $\lambda = e^{i\psi} \tanh r$

$$S_2(\xi)|0\rangle = \sqrt{1 - |\lambda|^2} \sum_{n=0}^{\infty} \lambda^n |n\rangle|n\rangle, \tag{D.6}$$

which is also referred to as twin-beam state (TWB), since a measurement of the photon number on the two beams always leads to the same result. Note that

$$|\lambda|^2 = \frac{N}{N+1}\,, \tag{D.7}$$

where $N = \sinh^2|\xi|$ is the average number of photon per mode.

Remarkably, if we consider a single beam of a TWB, it is a *thermal state* with average number of photons N and, thus, it is described by the density operator

$$\varrho(N) = \frac{1}{1+N}\sum_{n=0}^{\infty}\left(\frac{N}{1+N}\right)^n |n\rangle\langle n|. \tag{D.8}$$

The states of the form given in eq. (D.8) are called thermal states because they have the same analytical expression as the state describing a radiation of frequency ω at equilibrium at temperature T. In this last case, the average number of photons is

$$N_{\mathrm{th}} = \frac{1}{e^{\hbar\omega/(k_{\mathrm{B}}T)} - 1}\,, \tag{D.9}$$

where k_{B} is the Boltzmann constant. It is also interesting to note that, since the reduced state of the TWB is a thermal state, it exhibits the maximum von Neumann entropy for a fixed energy: being the TWB a pure state, this means that it is a maximally entangled state.

Appendix E.

Bernoulli sampling from non-unit efficiency photodetection

A photon-number-resolving detector allows to directly measure the photon number distribution

$$p(n) = \langle n|\varrho|n\rangle \tag{E.1}$$

of an input state ϱ and it is described by the projectors $|n\rangle\langle n|$ onto the photon number basis $\{|n\rangle\}$, with $n \in \mathbb{N}$.

However, a realistic detector has a non-unit quantum efficiency η, that can be seen as an overall loss of photons during the detection process. From the theoretical point of view, a real photodetector can be modelled as a beam splitter with transmissivity η followed by an ideal photon-number-resolving detector, as sketched in fig. 26. In this scheme, before the detection the input state is mixed with the vacuum state at the beam splitter and part of its photons is thus reflected and lost.

If we send a single-photon state $|1\rangle$ to the realistic detector, η corresponds to the probability of detection. What happens when we send a Fock state $|n\rangle$, $n > 1$? Starting from the model of fig. 26 and by using the results of appendix A, we can explicitly calculate the evolution of the two-mode input state $|n\rangle|0\rangle$ just after the beam splitter,

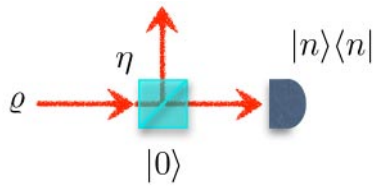

Fig. 26. – A photon-number-resolving detector with quantum efficiency η can be represented as an ideal photodetector and a beam splitter with transmissivity η in front of it. Note the presence of the vacuum state $|0\rangle$.

described by the unitary operator $U_{\rm BS}(\eta)$, namely

$$U_{\rm BS}(\eta)|n\rangle|0\rangle = \frac{1}{\sqrt{n!}}\left(\sqrt{\eta}\,a^\dagger - \sqrt{1-\eta}\,b^\dagger\right)^n |0\rangle, \tag{E.2a}$$

$$= \frac{1}{\sqrt{n!}}\sum_{k=0}^{n}\binom{n}{k}(-1)^k\sqrt{\eta^{n-k}(1-\eta)^k}\,(a^\dagger)^{n-k}(b^\dagger)^k|0\rangle, \tag{E.2b}$$

$$= \sum_{k=0}^{n}(-1)^k\sqrt{\binom{l}{k}\eta^{n-k}(1-\eta)^k}\,|l-k\rangle|k\rangle, \tag{E.2c}$$

$$= \sum_{m=0}^{n}(-1)^{h-m}\sqrt{\binom{n}{m}\eta^m(1-\eta)^{n-m}}\,|m\rangle|n-m\rangle, \tag{E.2d}$$

where we assumed that the states $|n\rangle$ and $|0\rangle$ refer to the modes described by the bosonic filed operators a and b, respectively. Therefore, the probability $P(m;\eta)$ to detect m photons, $m \leq n$, is given by

$$P(m;\eta) = \binom{n}{m}\eta^m(1-\eta)^{n-m}. \tag{E.3}$$

Of course, if $\eta \to 1$ we have $P(m;\eta) \to p(m) = \delta_{n,m}$.

It is now clear that if we know the *actual* photon number statistics $p(n)$ of the state ϱ, then the *detected* photon number statistics is

$$P(m;\eta) = \sum_{n=0}^{\infty}\binom{n}{m}\eta^m(1-\eta)^{n-m}p(n), \tag{E.4a}$$

$$= \sum_{n=0}^{\infty}\binom{n}{m}\eta^m(1-\eta)^{n-m}\langle n|\varrho|n\rangle. \tag{E.4b}$$

Exploiting this simple model based on the beam splitter, it is also straightforward to find the evolution of a quantum state ϱ through a dissipative channel: in this case the quantum efficiency should be replaced by the overall loss parameter.

REFERENCES

[1] Kwiat P. G., Mattle K., Weinfurter H., Zeilinger A., Sergienko A. V. and Shih Y., *Phys. Rev. Lett.*, **75** (1995) 4337.
[2] Cialdi S., Brivio D. and Paris M. G. A., *Phys. Rev. A*, **81** (2010) 042322.
[3] Bennett C. H. and Brassard G., in *Proceedings of IEEE International Conference on Computers, Systems and Signal Processing, Bangalore, India, 1984* (IEEE Press, New York) 1984, p. 175.
[4] Hu J.-Y., Yu B., Jing M.-Y., Xiao L.T., Jia S.-T., Qin G.-Q., and Long G.-L., *Light: Sci. Appl.*, **5** (2016) e16144.
[5] Giovannetti V., Lloyd S. and Maccone L., *Phys. Rev. Lett.*, **96** (2006) 010401.
[6] Roccia E., Gianani I., Mancino L., Sbroscia M., Somma F., Genoni M. G. and Barbieri M., *Quantum Sci. Technol.*, **3** (2018) 01LT01.
[7] Crespi A., Osellame R., Ramponi R., Brod D. J., Galvao E. F., Spagnolo N., Vitelli C., Maiorino E., Mataloni P. and Sciarrino F., *Nat. Photon.*, **7** (2013) 545.
[8] Spring J. B., Metcalf B. J., Humphreys P. C., Kolthammer W. S., Jin X.-M., Barbieri M., Datta A., Thomas-Peter N., Langford N. K., Kundys D., Gates J. C., Smith B. J., Smith P. G. R. and Walmsley A. I., *Science*, **339** (2013) 798.
[9] Dinani H. T. and Berry D. W., *Phys. Rev A*, **90** (2014) 023856.
[10] Weedbrook C., Pirandola S., Garcá-Patrón R., Cerf N. J., Ralph T. C., Shapiro J. H. and Lloyd S., *Rev. Mod. Phys.*, **84** (2012) 621.
[11] Adesso G., Ragy S. and Lee A. R., *Open Syst. Inf. Dyn.*, **21** (2014) 440001.
[12] Usenko V. C., Heim B., Peuntinger C., Wittmann C., Marquardt C., Leuchs G. and Filip R., *New J. Phys.*, **14** (2012) 093048.
[13] Vallone G., Bacco D., Dequal D., Gaiarin S., Luceri V., Bianco G. and Villoresi P., *Phys. Rev. Lett.*, **115** (2015) 040502.
[14] Allevi A., Lamperti M., Bondani M., Peřina J. Jr., Michálek V., Haderka O. and Machulka R., *Phys. Rev. A*, **88** (2013) 063807.
[15] Usenko V. C., Ruppert L. and Filip R., *Opt. Express*, **23** (2015) 31534.
[16] Silberhorn Ch., Korolkova N. and Leuchs G., *Phys. Rev. Lett.*, **88** (2002) 167902.
[17] Olivares S. and Paris M. G. A., *Int. J. Mod. Phys. B*, **27** (2013) 1345024.
[18] Paris M. G. A., *Int. J. Quantum Inf.*, **7** (2009) 125.
[19] Helstrom C. W., *Quantum Detection and Estimation Theory* (Academic, New York) 1976.
[20] Braunstein S. L. and Caves C. M., *Phys. Rev. Lett.*, **72** (1994) 3439.
[21] Braunstein S. L., Caves C. M. and Milburn G. J., *Ann. Phys. (NY)*, **247** (1996) 135.
[22] Brody D. C. and Hughston L. P., *Proc. R. Soc. London, Ser. A*, **454** (1998) 2445; **455** (1999) 1683.
[23] Szczykulska M., Baumgratz T. and Datta A., *Adv. Phys. X*, **1** (2016) 621.
[24] Brunelli M., Olivares S., Paternostro M. and Paris M. G. A., *Phys. Rev. A*, **86** (2012) 012125.
[25] Bina M., Amelio I. and Paris M. G. A., *Phys. Rev. E*, **93** (2016) 052118.
[26] Rossi M. A. C., Bina M., Paris M. G. A., Genoni M. G., Adesso G. and Tufarelli T., *Quantum Sci. Technol.*, **2** (2017) 01LT01.
[27] Genoni M. G., Olivares S. and Paris M. G. A., *Phys. Rev. Lett.*, **106** (2011) 153603.
[28] Genoni M. G., Olivares S., Brivio D., Cialdi S., Cipriani D., Santamato A., Vezzoli S. and Paris M. G. A., *Phys. Rev. A*, **85** (2012) 043817.
[29] Bina M., Grasselli F. and Paris M. G. A., *Phys. Rev. A*, **97** (2018) 012125.
[30] Tamascelli D., Benedetti C., Olivares S. and Paris M. G. A., *Phys. Rev. A*, **94** (2016) 042129.
[31] Rossi M. A. C., Giani T. and Paris M. G. A., *Phys. Rev. D*, **94** (2017) 024014.
[32] Seveso L., Peri V. and Paris M. G. A., *J. Phys A: Math. Theor.*, **50** (2017) 235301.
[33] Sparaciari C., Olivares S. and Paris M. G. A., *Phys. Rev. A*, **93** (2016) 023810.
[34] Glauber R. J., *Phys. Rev.*, **131** (1963) 2766.
[35] Abadie J. *et al.* (LIGO Scientific Collaboration), *Nat. Phys.*, **7** (2011) 962.

[36] Demkowicz-Dobrzański R., Jarzyna M. and Kołodyśky J., *Prog. Opt.*, **60** (2015) 345.
[37] Sparaciari C., Olivares S. and Paris M. G. A., *J. Opt. Soc. Am. B*, **32** (2015) 1354.
[38] Paris M. G. A., *Phys. Lett. A*, **201** (1995) 132.
[39] Olivares S. and Paris M. G. A., *Opt. Spectrosc.*, **103** (2007) 231.
[40] Pezzè L. and Smerzi A., *Phys. Rev. Lett.*, **100** (2008) 073601.
[41] Lang M. D. and Caves C. M., *Phys. Rev. Lett.*, **111** (2013) 173601.
[42] Kok P. *et al.*, *Phys. Rev. A*, **63** (2001) 063407.
[43] Olivares S., Popovic M. and Paris M. G. A., *Quantum Meas. Quantum Metrol.*, **3** (2016) 38.
[44] Bachor H.-A. and Ralph T. C., *A Guide to Experiments in Quantum Optics* (Wiley-VCH, New York) 2004.
[45] D'Auria V., Fornaro S., Porzio A., Solimeno S., Olivares S. and Paris M. G. A., *Phys. Rev. Lett.*, **102** (2009) 020502.
[46] Cialdi S., Porto C., Cipriani D., Olivares S. and Paris M. G. A., *Phys. Rev. A*, **93** (2016) 043805.
[47] Olivares S., *Eur. Phys. J. ST*, **203** (2012) 3.
[48] Yurke B., McCall S. L. and Klauder J. R., *Phys. Rev. A*, **33** (1986) 4033.
[49] Plick W. N., Dowling J. P. and Agarwal G. S., *New J. Phys.*, **12** (2010) 083014.
[50] Demkowicz-Dobrzański R., Banaszek K. and Schnabel R., *Phys. Rev. A*, **88** (2013) 041802(R).
[51] Lloyd S., *Science*, **321** (2008) 1463.
[52] Tan S., Erkmen B., Giovannetti V., Guha S., Lloyd S., Maccone L., Pirandola S. and Shapiro J. H., *Phys. Rev. Lett.*, **101** (2008) 253601.
[53] Shapiro J. H. and Lloyd S., *New J. Phys.*, **11** (2009) 063045.
[54] Shapiro J. H., *Phys. Rev. A*, **80** (2009) 022320.
[55] Meda A., Losero E., Samantaray N., Scafirimuto F., Pradyumna S., Avella A., Ruo-Berchera I. and Genovese M., *J. Opt.*, **19** (2017) 094002.
[56] Brida G., Genovese M. and Ruo Berchera I., *Nat. Photon.*, **4** (2010) 227.
[57] Lopaeva E. D., Ruo Berchera I., Degiovanni I. P., Olivares S., Brida G. and Genovese M., *Phys. Rev. Lett.*, **110** (2013) 153603.
[58] Lopaeva E. D., Ruo Berchera I., Olivares S., Brida G., Degiovanni I. P. and Genovese M., *Phys. Scr.*, **T160** (2014) 014026.
[59] Ragy S., Ruo Berchera I., Degiovanni I. P., Olivares S., Paris M. G. A., Adesso G. and Genovese M., *J. Opt. Soc. Am. B*, **31** (2014) 2045.
[60] Olivares S. and Paris M. G. A., *Metrologia*, **49** (2012) L14.
[61] Barzanjeh S., Guha S., Weedbrook C., Vitali D., Shapiro J. H. and Pirandola S., *Phys. Rev. Lett.*, **114** (2015) 080503.
[62] Zhuang Q., Zhang Z. and Shapiro J. H., *Phys. Rev. A*, **96** (2017) 020302(R).
[63] Giovannetti V., Lloyd S. and Maccone L, *Nat. Photon.*, **5** (2011) 22.
[64] Samantaray N., Ruo-Berchera I., Meda A. and Genovese M., *Light: Sci. Appl.*, **6** (2017) e17005.
[65] Ruo Berchera I., Degiovanni I. P., Olivares S. and Genovese M., *Phys. Rev. Lett.*, **110** (2013) 213601.
[66] Ruo Berchera I., Degiovanni I. P., Olivares S., Samantaray N., Traina P. and Genovese M., *Phys. Rev. A*, **92** (2015) 053821.
[67] Benatti F., Floreanini R., Olivares S. and Sindinci E., *Int. J. Quantum Inf.*, **15** (2017) 1740014.
[68] Aschieri P. and Castellani L., *J. High Energy Phys.*, **06** (2009) 086.
[69] Aschieri P. and Castellani L., *J. Geom. Phys.*, **60** (2010) 375.
[70] Pikovski I., Vanner M. R., Aspelmeyer M., Kim M. S. and Brukner Č., *Nat. Phys.*, **8** (2012) 393.
[71] Hogan G., *Phys. Rev. D*, **85** (2012) 064007.
[72] Chou A. S. *et al.* (Holometer Collaboration), *Phys. Rev. Lett.*, **117** (2016) 111102.
[73] Caves C. M., *Phys. Rev. D*, **23** (1981) 1693.